Research Square

Preprints are preliminary reports that have not undergone peer review.
They should not be considered conclusive, used to inform clinical practice,
or referenced by the media as validated information.

Federated Scientific Machine Learning Framework for Multi-Scale Inverse Parameter Identification: Application to Nonlocal Strain Gradient Plasticity

George Z. Voyiadjis

voyiadjis@eng.lsu.edu

Louisiana State University

Babur Deliktas

Bursa Uludag University

Aiman Tariq

Bursa Uludag University

Research Article

Keywords: Federated learning, strain gradient plasticity, nonlocal model, inverse method, parameter identification, scientific machine learning

Posted Date: August 25th, 2026

DOI: https://doi.org/10.21203/rs.3.rs-10706047/v1

License: This work is licensed under a Creative Commons Attribution 4.0 International License.
Read Full License

Additional Declarations: No competing interests reported.

Federated Scientific Machine Learning Framework for Multi-Scale Inverse Parameter Identification: Application to Nonlocal Strain Gradient Plasticity

George Voyiadjis [a,*], Babür Deliktaş [b] and Aiman Tariq [c]

[a] *Computational Solid Mechanics Laboratory, Department of Civil and Environmental Engineering, Louisiana State University, Baton Rouge, LA 70803, USA*
[b, c] *Artificial Intelligence and Computational Mechanics Laboratory, Department of Civil Engineering, Bursa Uludag University, Bursa, 16059, Türkiye*

Abstract

Size-dependent plasticity in micro-scale experiments cannot be adequately described by classical plasticity, while calibration of nonlocal strain gradient plasticity (SGP) models remains challenging due to sparse and geometry-dependent experimental data. In this study, we develop, for the first time, an inverse federated scientific machine learning (I-FedSciML) framework for identifying parameters of a size-dependent nonlocal SGP model without centralizing raw experimental data. Each experimental curve is treated as an independent client characterized by its own geometry, microstructural length scale, loading mode, and measured response. A geometry-conditioned inverse neural network maps client descriptors to the SGP parameter vector, which is then embedded in differentiable micro-bending and micro-torsion SGP forward models. We validated the framework using micro-scale experimental datasets for annealed nickel beams, LIGA nickel foils, aluminum beams, and copper wires. The identified client-specific parameters accurately reproduce experimental moment–curvature and torque–twist responses, with R^2 values of 0.982–0.990 for annealed nickel, 0.925–0.974 for LIGA nickel, 0.898–0.904 for aluminum, and 0.985–0.997 for copper torsion. Noise sensitivity analysis at 1%, 2.5%, 5%, and 10% showed that although parameter bias, prediction uncertainty, and the final loss plateau increase with noise level, the framework maintains reliable predictive capability even at 10% noise. These results demonstrate that I-FedSciML provides an effective and privacy-preserving route for collaborative calibration of nonlocal size-dependent constitutive models.

Keywords: Federated learning, strain gradient plasticity, nonlocal model, inverse method, parameter identification, scientific machine learning

* *Corresponding author*

[a] *email address:* voyiadjis@eng.lsu.edu ORCID ID: 0000-0002-7965-6592
[b] *email address:* bdeliktas@uludag.edu.tr ORCID ID: 0000-0002-4035-4642
[c] *email address:* aimantariq@uludag.edu.tr ORCID ID: 0000-0003-0369-9091

August 14, 2026

1. Introduction

Strain gradient plasticity (SGP) is among an essential theoretical framework for describing size-dependent plastic deformation at the micro- and sub-micro scales. Classical plasticity does not contain an intrinsic material length scale and therefore cannot capture the experimentally observed strengthening that occurs when characteristic specimen dimensions approach the scale of microstructural features. This limitation is especially evident in micro-bending, micro-torsion, indentation, thin films, and micron-scale metallic structures, where plastic strain gradients promote the accumulation of geometrically necessary dislocations (GNDs) in addition to statistically stored dislocations (SSDs). Foundational contributions by Aifantis (1984), Fleck and Hutchinson (1993, 1997), Fleck et al. (1994), Nix and Gao (1998), Gao et al. (1999), Huang et al. (2000), Gudmundson (2004), and Gurtin and Anand (2005) established the theoretical basis for incorporating gradient effects into continuum plasticity. Building on these developments, Voyiadjis and co-workers further advanced thermodynamically consistent gradient-enhanced continuum plasticity formulations to improve the prediction of material behavior across different length scales (Dorgan and Voyiadjis, 2003; Voyiadjis and Al-Rub, 2007; Voyiadjis and Deliktas, 2009; Faghihi and Voyiadjis, 2012; Voyiadjis and Faghihi, 2014; Song and Voyiadjis, 2018; Voyiadjis and Song 2019). Additionally, some recent strain gradient studies include those of Tariq et al., (2024), Xie et al., (2025).

Although many SGP formulations introduce a material length scale to represent the influence of plastic strain gradients, treating this length scale as a fixed constant may not be sufficiently general. The effective length scale can depend on grain size, specimen size, plastic strain level, hardening behavior, and deformation mode. This was addressed by Voyiadjis and Abu Al-Rub (2005), who proposed a generalized gradient plasticity model with a non-fixed length-scale parameter motivated by dislocation mechanics. Their formulation provides a more flexible description of size effects by allowing the intrinsic length scale to evolve with microstructural and deformation variables. However, this increased physical flexibility also introduces additional calibration challenges. The model response depends on several interdependent parameters, including the reference stress, hardening modulus, hardening exponent and the evolving length-scale relation. Accurate identification of these parameters is therefore critical for predicting the size-dependent response of different micro-scale bending and torsion experiments.

The calibration of constitutive model parameters is commonly formulated as an inverse problem, where the unknown material parameters are inferred by minimizing the discrepancy between experimental measurements and model predictions. Classical inverse identification approaches include Finite Element Model Updating (FEMU) (Kavanagh et al., 1971), Virtual Fields Method (VFM) (Grédiac, 1989), Constitutive Equation Gap Method (CEGM) (Ladevèze & Leguillon, 1983), Equilibrium Gap Method (EGM) (Claire et al., 2004), Integrated Digital Image Correlation method (Integrated-DIC) (Réthoré, 2010), Dissipation Gap Method (DGM) (Blaysat et al., 2012), Self-Optimizing Method (Self-OPTIM) (Yun & Shang, 2011), and Constitutive Compatibility Method (CCM) (Moussawi et al., 2013). More recent studies have introduced automatic differentiation, Bayesian calibration, and machine-

learning-assisted optimization to improve computational efficiency and uncertainty quantification in inverse constitutive modeling (Martins et al., 2018; Seidl and Granzow, 2022; Bastos et al., 2022; Andrade-Campos et al., 2022; Gaynutdinova et al., 2023; Tariq and Deliktaş, 2025; Kapcı et al., 2026; Polat et al., 2026). However, inverse identification becomes significantly more difficult for nonlocal and gradient-enhanced plasticity models because the response depends not only on local stress–strain behavior but also on geometry, strain gradients, microstructural length scales, and higher-order coupling terms.

Several studies have applied SGP and related nonlocal models to interpret micro-bending, micro-torsion, indentation, and fracture experiments. Voyiadjis et al. (2023) examined the combined influence of microstructure and geometry on the deformation behavior and energy absorption of LPBF-manufactured Inconel 718 hexagonal honeycomb structures through miniature tensile and compression testing. Niordson and Hutchinson (2003), Wang et al. (2018), Begley and Hutchinson (1998), Bardella and Panteghini (2015), Martínez-Pañeda et al. (2016), Liu et al. (2012), Gan et al. (2014), and Guo et al. (2017) demonstrated that strain-gradient effects can substantially modify the apparent strength of micron-scale structures. These works have been essential in validating gradient plasticity concepts; however, most parameter identification procedures are still performed independently for each dataset or test configuration. As a result, the information contained in multiple related experiments is rarely exploited in a unified inverse calibration framework. This is a limitation because micro-scale datasets are often sparse, heterogeneous, and obtained under different geometries, loading modes, or laboratory conditions. Independent calibration may therefore lead to parameter non-uniqueness, and limited insight into the geometry dependence of the identified SGP parameters.

On the other hand, scientific machine learning (SciML) offers a promising route for overcoming some of these limitations by combining data-driven learning with physics-based modeling (Kirchdoerfer and Ortiz, 2016; Mozaffar et al., 2019; As'ad et al., 2022; Rezaei et al., 2024). Recently physics-informed neural networks (PINNs) introduced by Raissi et al. (2019), and physics-guided ML models have demonstrated remarkable capabilities in capturing nonlinear and path-dependent material behaviors (Cai et al., 2021; Ling et al., 2024; Polat et al., 2025; Moon et al., 2025; Tariq et al., 2026). For example, Lourenço et al. (2025) developed recurrent neural network (RNN) models trained on centralized datasets, where phenomenological constraints were embedded to improve predictive capability. Similarly, Tariq et al. (2025) and Kadioglu et al. (2025) demonstrated that a suitable ML model can effectively analyze the torsional vibration behavior of viscoelastic nanotubes yet remains robust under increasing noise levels. Flaschel et al. (2021), Thakolkaran et al. (2022) and Flaschel et al. (2023) introduced an unsupervised model discovery framework (EUCLID) for hyperelastic materials, where the physical principles are incorporated directly into the loss function through regularization terms, enabling the model to be trained without requiring explicit stress labels. Overall, these studies demonstrate that neural networks can be used either as direct constitutive surrogates, thermodynamically constrained material models, operator-learning tools, or inverse solvers.

Federated learning provides an additional capability that is highly relevant to scientific and engineering datasets distributed across different laboratories, institutions, or industrial

partners. In federated learning, multiple clients collaboratively train a shared model without transferring raw data to a central repository. Instead, each client performs local training and communicates only model updates to a central server, where they are aggregated. This concept was formalized by McMahan et al. (2017) and has since been extended to address non-IID data, client heterogeneity, communication efficiency, and adaptive optimization through works such as Yang et al. (2019), Li et al. (2020a), Karimireddy et al. (2020), Kairouz and McMahan (2021). More recently, federated scientific machine learning has emerged as a natural extension of this idea, where machine learning models are trained over distributed scientific datasets. Recent developments such as physics-informed decentralized federated learning demonstrate that federated training can be combined with physics-based learning to solve differential equations and scientific inverse problems under data heterogeneity (Zhang et al., 2024; Alfano et al., 2025).

Despite these advances, the use of federated scientific machine learning for inverse identification of nonlocal SGP parameters remains largely unexplored. This gap is important because SGP calibration naturally involves heterogeneous datasets: each experiment may have a different grain size, specimen size, loading mode, strain-gradient distribution, and measured response. At the same time, all datasets may be governed by the same underlying nonlocal plasticity theory. This creates an ideal setting for federated inverse learning, where each experiment can be treated as an independent client, while a shared inverse model learns from all clients through weight aggregation. Such a framework is particularly useful when experimental data are distributed across different research groups or when direct sharing of raw data is restricted by ownership, confidentiality, or practical limitations.

The present study addresses this gap by developing an inverse federated scientific machine learning (I-FedSciML) framework for multi-scale parameter identification in nonlocal strain gradient plasticity. The proposed framework treats each experimental micro-bending or micro-torsion curve as an independent federated client. Each client is characterized by its own geometric descriptors, microstructural scale, loading type, and measured response. A shared geometry-conditioned inverse neural network maps the client descriptor to a client-specific SGP parameter vector. These parameters are then inserted into a differentiable SGP forward model to predict the corresponding bending or torsion response. The local client loss is computed from the discrepancy between the predicted and experimental response, while the global model is updated using FedAvg. The neural network does not replace the SGP theory; instead, it serves as an inverse parameter-identification operator constrained by the physics-based forward model.

The main contribution of this work is the development of a geometry-conditioned inverse federated framework that can identify client-specific SGP parameters from multiple heterogeneous micro-scale experiments without centralizing raw experimental data. The framework is evaluated using four representative benchmark cases: micro-bending of thin annealed nickel beams, micro-bending of LIGA nickel foils, micro-bending of aluminum beams, and micro-torsion of thin copper wires. Through these examples, we intend to demonstrate that the proposed I-FedSciML framework can recover distinct geometry-dependent parameter sets, reproduce experimental moment–curvature and torque–twist responses, and provide insight into parameter sensitivity across different size-dependent

plasticity problems. More broadly, the proposed methodology establishes a foundation for collaborative constitutive model calibration across distributed laboratories and heterogeneous experimental platforms while preserving the interpretability of nonlocal strain gradient plasticity.

2. Methodology

This section presents the theoretical formulation of strain gradient plasticity used in the present study. First, Section 2.1 introduces the generalized strain gradient plasticity model with a varying material length scale. The subsequent subsections then apply this nonlocal formulation to size-dependent micro-bending and micro-torsion problems, where the governing response equations for thin beams and wires are derived.

2.1. Strain Gradient Plasticity Model with Varying Length Scale

The intrinsic material length scale plays a central role in strain gradient plasticity theories, since it controls the contribution of strain gradients and enables the description of size-dependent plastic deformation. In many conventional gradient plasticity formulations, this length scale is treated as a fixed material parameter. However, the use of a constant length scale may not be sufficiently general, particularly when the mechanical response is influenced by microstructural features, specimen size, or loading configuration. In addition, the interaction between the conventional local hardening contribution and the nonlocal gradient-dependent contribution is not necessarily linear. Different materials and deformation problems may require different forms of coupling between these two mechanisms. In this regard, Voyiadjis and Abu Al-Rub (2005) proposed a generalized strain gradient plasticity model in which the material length scale is not fixed but is instead formulated based on dislocation mechanics and microstructural characteristics.

In gradient plasticity, the nonlocal or gradient-enhanced effective plastic strain ($\hat{p}$) is commonly introduced as the internal hardening variable conjugate to isotropic plastic hardening. This quantity combines the local effective plastic strain p with a higher-order strain-gradient measure η. A generalized form of the nonlocal effective plastic strain can be written as (Voyiadjis and Abu Al-Rub, 2005)

$$\hat{p} = [f(p)^{\gamma_1} + g(\ell^n \eta_n)^{\gamma_2}]^{1/\gamma_3} \tag{1}$$

where ℓ is the material length-scale parameter and n is associated with the order of the gradient measure used in η. The function $f(p)$ represents the contribution of the local plastic strain, whereas $g(\ell^n \eta_n)$ represents the contribution of the effective plastic strain gradient. The coefficients γ_1, γ_2, and γ_3 are the interaction coefficients, controlling the interaction between the local and gradient-dependent hardening terms. Voyiadjis and Abu Al-Rub (2005) introduced a more general hardening relation capable of incorporating experimentally observed size effects in micro-scale plasticity problems. The corresponding flow stress relation is expressed as follows,

$$\sigma_f = \sigma_{ref} + \sigma_0[f(p)^{\gamma_1} + (\ell\eta_1 + \ell^2\eta_2)^{\gamma_2}]^{1/m\gamma_3} \quad (2)$$

where σ_{ref}, σ_0, and m are the reference (yield) stress, hardening modulus, and hardening exponent, respectively. The quantities η_1 and η_2 denote first- and second-order effective plastic strain-gradient measures. This flow stress relation in is not a purely phenomenological expression. Rather, it is motivated by dislocation mechanics and provides a physically based means of incorporating both conventional strain hardening and strain-gradient-induced hardening into a single constitutive relation. For von Mises plasticity, the flow stress may be identified with the effective stress as $\sigma_f = \sigma_{eff} = \sqrt{3\sigma'_{ij}\sigma'_{ij}/2}$ where σ'_{ij} is the deviatoric stress tensor.

Subsequently using the definitions for effective plastic strain $\left(p = \sqrt{2\varepsilon_{ij}\varepsilon_{ij}/3}\right)$ together with the deviatoric stress tensor $\left(\sigma'_{ij} = \sigma_{ij} - \sigma_{kk}\delta_{ij}/3\right)$ and assuming that the deviatoric stress tensor is proportional to the corresponding strain-like tensor $\left(\sigma'_{ij} = \lambda\varepsilon_{ij}\right)$, the proportionality coefficient can be obtained by enforcing consistency with the von Mises effective stress definition. This leads to the following relation

$$\sigma'_{ij} = \frac{2\sigma_f}{3p}\varepsilon_{ij} \quad (3)$$

Voyiadjis and Abu Al-Rub (2005) adopted an evolution equation for the material length scale that is consistent with the experimental trends and depends on the plastic strain p, the hardening exponent m, specimen size h, and the grain size d. The expression for length scale parameter takes the following form

$$\ell = \frac{hd}{h + d(p)^{1/m}} \quad (4)$$

2.2. Size-Dependent Bending of Thin Beams

The size-dependent strengthening observed in micro-scale bending cannot be captured by classical plasticity theory, since it does not include an intrinsic material length scale. To quantify this length-scale effect experimentally, several researchers have developed micro-bending tests on thin metallic beams and foils. Stölken and Evans (1998) first introduced a micro-bending test method using 99.99% pure annealed nickel foils, which was later adopted by Shrotriya et al. (2003) for polycrystalline LIGA nickel foils. Haque and Saif (2003) subsequently performed bending experiments on aluminum micro-cantilever beams. A schematic representation of the experimental setup is shown in Figure 1. The results of these studies consistently demonstrated a pronounced size effect i.e., thinner beams exhibit higher normalized bending resistance, whereas the bending strength decreases as the beam thickness increases. This behavior provides clear evidence of strain-gradient hardening and motivates the use of strain gradient plasticity models with an intrinsic material length scale.

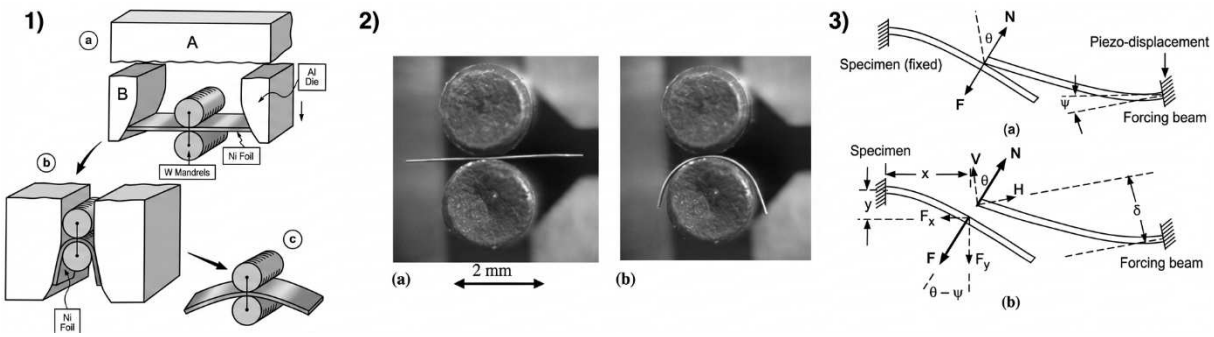


Figure 1. Schematic illustration of the micro-bending experimental configurations reported by 1) Stolken and Evans (1998), 2) Shrotriya et al. (2003) and 3) Haque and Saif (2003).

For pure bending of a thin beam in the $x_1 - x_2$ plane, let x_1 denote the beam axis and x_2 the thickness coordinate measured from the neutral axis. Under the isochoric two-dimensional deformation (plastic deformation is assumed to be incompressible), the displacement field is written as

$$u_1(x_1, x_2) = -\kappa x_1 x_2, \qquad u_2(x_1, x_2) = \frac{\kappa}{2}(x_1^2 + x_2^2), \qquad u_3(x_1, x_2) = 0 \tag{5}$$

where κ is the applied curvature. The corresponding strain components are

$$\varepsilon_{11} = \frac{\partial u_1}{\partial x_1} = -\kappa x_2, \qquad \varepsilon_{22} = \frac{\partial u_2}{\partial x_2} = \kappa x_2, \quad \gamma_{12} = 0 \tag{6}$$

Using Equation (6) into effective plastic strain $p = \sqrt{2\varepsilon_{ij}\varepsilon_{ij}/3}$, the bending strain field gives

$$p = \sqrt{\frac{2}{3}\{(-\kappa x_2)^2 + (\kappa x_2)^2\}} \tag{7}$$

$$p = \frac{2}{\sqrt{3}}\kappa|x_2| \tag{8}$$

Subsequently, the effective strain gradients $\eta_1 = \sqrt{\nabla p . \nabla p}$ and $\eta_2 = \nabla^2 p$ can be expressed as

$$\eta_1 = \frac{2}{\sqrt{3}}\kappa, \qquad \eta_2 = \nabla^2 p = 0 \tag{9}$$

By substituting Equations (8) and (9) into Equation (2), one can obtain the generalized SGP flow stress relation as

$$\sigma_f = \sigma_{ref} + \sigma_0 \left[\left(\frac{2}{\sqrt{3}}\kappa|x_2| \right)^{\gamma_1} + \left(\ell \frac{2}{\sqrt{3}}\kappa \right)^{\gamma_2} \right]^{1/m\gamma_3} \tag{10}$$

Now substituting this equation with variables such as $y = x_2/h$, $\beta = \ell/h$, $\varepsilon_s = \kappa h$ and $n = 1/m\gamma_3$ leads to the following equation

$$\sigma_f = \sigma_{ref} + \sigma_0 \left[\left(\frac{2}{\sqrt{3}}\varepsilon_s|y| \right)^{\gamma_1} + \left(\frac{2}{\sqrt{3}}\beta\varepsilon_s \right)^{\gamma_2} \right]^{n} \tag{11}$$

The bending moment M can be obtained by integrating the normal stress contribution $\sigma_{11} = 2\sigma_f x_2/\sqrt{3}|x_2|$ over the beam cross-section as

$$M = \frac{2b}{\sqrt{3}} \int_{-h/2}^{h/2} \sigma_f \, |x_2| dx_2 \tag{12}$$

where b is the beam width. Introducing $x_2 = yh$, $dx_2 = hdy$ and $y \in [-1/2\,, 1/2]$ into Equation (12)

$$M = \frac{2bh^2}{\sqrt{3}} \int_{-1/2}^{1/2} \sigma_f \, |y| dy \tag{13}$$

Because the integrand is symmetric about the neutral axis, the bending moment can be rewritten by substituting Equation (11) into Equation (13) as

$$M = \frac{4bh^2}{\sqrt{3}} \int_0^{1/2} \left\{ \sigma_{ref} + \sigma_0 \left[\left(\frac{2}{\sqrt{3}} \varepsilon_s |y| \right)^{\gamma_1} + \left(\frac{2}{\sqrt{3}} \beta \;\; \varepsilon_s \right)^{\gamma_2} \right]^n \right\} y dy \tag{14}$$

To obtain local moment (M_0) where the length-scale contribution vanishes ($\ell \to 0$), Equation (14) reduces to

$$M_0 = \frac{4bh^2}{\sqrt{3}} \int_0^{1/2} \left\{ \sigma_{ref} + \sigma_0 \left[\left(\frac{2}{\sqrt{3}} \varepsilon_s |y| \right)^{\gamma_1} \right]^n \right\} y dy \tag{15}$$

Further solving this and using $a = \gamma_1 n$ leads to the following equation

$$M_0 = \frac{bh^2}{\sqrt{3}} \left[\frac{\sigma_{ref}}{2} + \frac{\sigma_0}{a+2} \left(\frac{\varepsilon_s}{\sqrt{3}} \right)^a \right] \tag{16}$$

Implementing the length scale parameter (Equation 4) into the β variable, provides the expression as

$$\beta = \frac{\ell(y)}{h} = \frac{d}{h + d \left(\frac{2}{\sqrt{3}} \varepsilon_s |y| \right)^{1/m}} \tag{17}$$

Since the dependency of β on y (i.e., β varies through the thickness), the governing equation does not admit a simple closed-form expression, unlike the local bending moment expression obtained for fixed length scale case in Equation (16). Therefore, one can use the exact numerical integration method such as trapezoidal method to discretize thickness and compute integrand point wise using following relation

$$I = \int (\cdot) dy \approx \text{trapz} \tag{18}$$

This numerical integration can capture full spatial variation of $\ell(y)$ and accurate gradient effects. Alternatively, one can use Hypergeometric Approximation to express Equation (14) in closed-form expression by assuming fixed length scale ($\ell(y) \approx \ell$). Hence, defining following setting for the terms in Equation (14)

$$A = \left(\frac{2}{\sqrt{3}}\varepsilon_s\right)^{\gamma_1} \qquad B = \left(\frac{2}{\sqrt{3}}\beta\ \ \varepsilon_s\right)^{\gamma_2} \tag{19}$$

The moment equation can be rewritten as

$$M = \frac{4}{\sqrt{3}}\int_0^{1/2} \sigma_{ref}\, y dy + \frac{4}{\sqrt{3}}\sigma_0 \int_0^{1/2} y(Ay^{\gamma_1} + B)^n dy \tag{20}$$

Integration of the first part is

$$\frac{4}{\sqrt{3}}\int_0^{1/2} \sigma_{ref}\, y dy = \frac{\sigma_{ref}}{2\sqrt{3}} \tag{21}$$

Integration of the second part is expressed as closed-form expression by Hypergeometric approximation

$$\frac{4}{\sqrt{3}}\sigma_0 \int_0^{1/2} y(Ay^{\gamma_1} + B)^n dy = \frac{\sigma_0}{2\sqrt{3}} B^n F_1\left(-n, \frac{2}{\gamma_1}; 1 + \frac{2}{\gamma_1}; -\frac{A}{B}\left(\frac{1}{2}\right)^{\gamma_1}\right) \tag{22}$$

Then Gauss hypergeometric function in Equation (22) with

$$n = \frac{1}{m\gamma_3}, \quad z = -\frac{\left(\frac{\varepsilon_s}{\sqrt{3}}\right)^{\gamma_1}}{\left(\frac{2}{\sqrt{3}}\beta\ \ \varepsilon_s\right)^{\gamma_2}} \tag{23}$$

can be simplified as

$$= F_1\left(-\frac{1}{m\gamma_3}, \frac{2}{\gamma_1}; 1 + \frac{2}{\gamma_1}; z\right) \tag{24}$$

2.3. Size-Dependent Torsion of Thin Wires

In torsion of circular wires, the shear strain varies along the radial direction from the twist axis. This radial variation produces strain gradients and promotes the formation of geometrically necessary dislocations (GNDs). As a result, the torsional hardening response is governed by the combined contributions of statistically stored dislocations (SSDs) and GNDs (Fleck et al., 1994). This mechanism makes micro-torsion a distinct and important test configuration for examining size-dependent plasticity. Voyiadjis and Kattan (1992) investigated the effect of different spin tensors in finite elasto-plastic analyses of various torsion problems involving hollow and solid cylindrical bars. Liu et al. (2013), Gan et al. (2014), and Guo et al. (2017) investigated strain-gradient-induced size effects in micro-scale metallic wires using automated torsion testing systems, as schematically shown in Figure 2. They reported that the identified material length scales vary within the range of approximately 2.05–4.02 μm. This variation indicates that the intrinsic length scale should not necessarily be treated as a fixed constant. Rather, it may depend on the material microstructure and its evolution during plastic deformation, as also emphasized by Abu Al-Rub and Voyiadjis (2006).

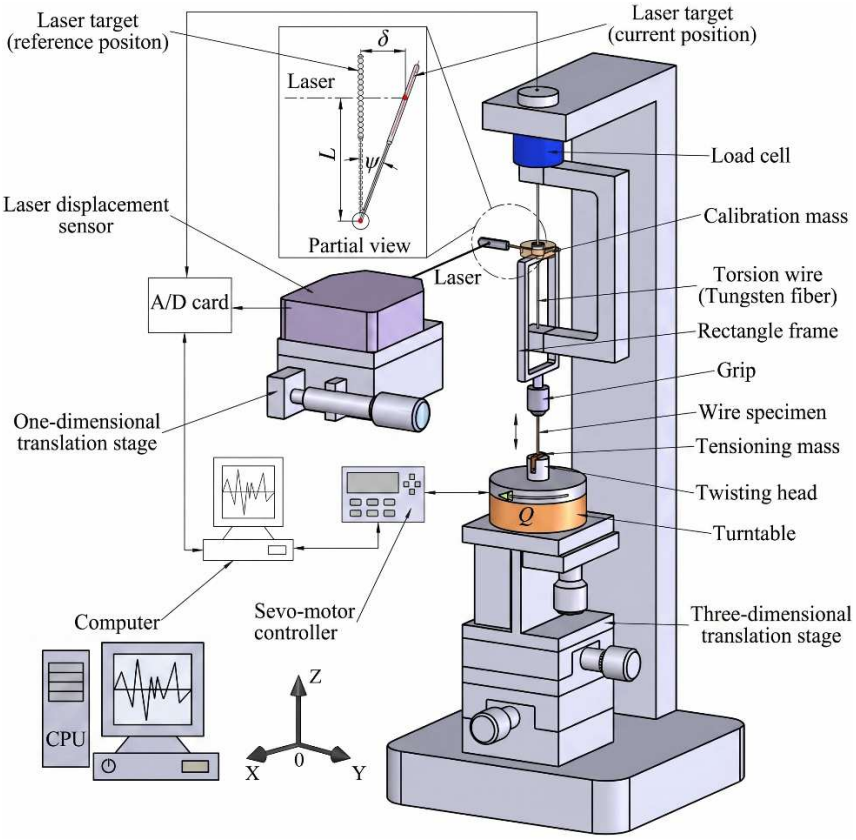


Figure 2. Schematic illustration of the single-wire miro-torsion test equipment reported by (Liu et al., 2013).

Voyiadjis and Abu Al-Rub (2005) applied the generalized strain gradient plasticity model to describe the size-dependent torsional response of thin wires. A Cartesian coordinate system is introduced such that $x_1$and x_2 lie in the cross-sectional plane of the wire, while x_3 coincides with the wire axis. The twist per unit length is denoted by κ, and the wire radius is a. For classical torsion, the displacement field may be written as

$$u_1(x_2, x_3) = -\kappa x_2 x_3, \qquad u_2(x_1, x_2) = \kappa x_1 x_3, \qquad u_3 = 0 \tag{25}$$

The corresponding non-zero strain components are

$$\varepsilon_{13} = \varepsilon_{31} = -\frac{1}{2}\kappa x_2, \;\; \varepsilon_{23} = \varepsilon_{32} = \frac{1}{2}\kappa x_1, \;\; \varepsilon_{11} = \varepsilon_{22} = \varepsilon_{22} = 0 \tag{26}$$

Under proportional loading, the local effective plastic strain p and the associated strain-gradient measures (η_1 and η_2) are expressed as

$$p = \frac{1}{\sqrt{3}}\kappa r\,, \quad \eta_1 = \frac{1}{\sqrt{3}}\kappa, \qquad \eta_2 = \frac{1}{\sqrt{3}}\kappa\frac{1}{r} \tag{27}$$

where $r = \sqrt{x_1^2 + x_2^2}$, is the radial coordinate. Following the deformation theory of plasticity, the deviatoric stress tensor is related to the strain tensor through $\sigma'_{ij} = 2\sigma_f \varepsilon_{ij}/3p$. Thus, the non-zero shear stress components are

$$\sigma'_{13} = \sigma'_{31} = \frac{2\sigma_f}{3p}\varepsilon_{13}, \qquad \sigma'_{23} = \sigma'_{32} = \frac{2\sigma_f}{3p}\varepsilon_{23} \tag{28}$$

Substituting the torsional strain and strain-gradient measures (Equation 27) into the generalized SGP flow stress relation (Equation 2) gives

$$\sigma_f = \sigma_{ref} + \sigma_0 \left[\left(\frac{1}{\sqrt{3}} \kappa r \right)^{\gamma_1} + \left(\frac{\ell}{\sqrt{3}} \kappa \right)^{\gamma_2} \left(1 + \frac{\ell}{r} \right)^{\gamma_2} \right]^{1/m\gamma_3} \tag{29}$$

The torque is then obtained by integrating the contribution of the shear stresses (σ'_{13} and σ'_{23}) over the circular cross-section:

$$Q = \frac{2\pi}{\sqrt{3}} \int_0^a \sigma_f \, r^2 dr \tag{30}$$

Using Equation (29) into Equation (30) leads to

$$Q = \frac{2\pi}{\sqrt{3}} \int_0^a \sigma_{ref} + \sigma_0 \left[\left(\frac{1}{\sqrt{3}} \kappa r \right)^{\gamma_1} + \left(\frac{\ell}{\sqrt{3}} \kappa \right)^{\gamma_2} \left(1 + \frac{\ell}{r} \right)^{\gamma_2} \right]^{1/m\gamma_3} r^2 dr \tag{31}$$

To account for the evolution of the intrinsic material length scale, the length-scale parameter is written as

$$\ell = \frac{ad}{a + d(p)^{1/m}} \tag{32}$$

Introducing the normalized radial coordinate $y = r/a$ and $\varepsilon_s = \kappa a$, the torque expression becomes

$$Q = \frac{2\pi \, a^3}{\sqrt{3}} \int_0^1 \sigma_{ref} + \sigma_0 \left[\left(\frac{\varepsilon_s}{\sqrt{3}} y \right)^{\gamma_1} + \left(\frac{\ell(y)}{\sqrt{3}} \frac{\varepsilon_s}{a} \right)^{\gamma_2} \left(1 + \frac{\ell(y)}{ay} \right)^{\gamma_2} \right]^{1/m\gamma_3} y^2 dy \tag{33}$$

Here, $\ell(y)$ depends on the radial coordinate through the local effective strain p. Consequently, as in the bending formulation, the governing torque integral generally does not reduce to a simple closed-form expression. The response is therefore evaluated numerically by discretizing the normalized radius and integrating the torque contribution pointwise across the wire cross-section.

3. I-FedSciML for Multi-Scale Parameter Identification

This section presents the fundamentals of I-FedSciML framework adopted for distributed inverse parameter identification. Section 3.1 first presents the general federated learning formulation, with emphasis on the Federated Averaging algorithm used to train a shared model across multiple decentralized clients. The discussion focuses on local client optimization, server-side parameter aggregation, and the suitability of federated learning for heterogeneous experimental datasets. Section 3.2 then adapts this framework to the inverse identification of the strain gradient plasticity parameters introduced in the previous sections.

3.1. An Overview of I-FedSciML

Federated learning is a distributed model-training strategy that allows multiple independent parties, such as industrial collaborators or research institutions, to jointly develop a predictive model without transferring their raw data to a central repository (Li et al., 2020b; Zhang et al., 2021; Wen et al., 2023). Under this framework, each participant keeps its dataset locally and carries out model training on its own data. Instead of sharing the data, the participants transmit only the model parameters, such as weights and biases, to a central server. These parameters are then combined, commonly through weighted averaging, to generate an improved global model (Deliktaş et al., 2026). The updated global model is subsequently sent back to the clients, where it is further refined through additional rounds of local training and global aggregation. This makes federated learning especially useful when privacy requirements, security issues, or proprietary limitations prevent direct data exchange. The general workflow of the federated machine learning is shown in Figure 3.

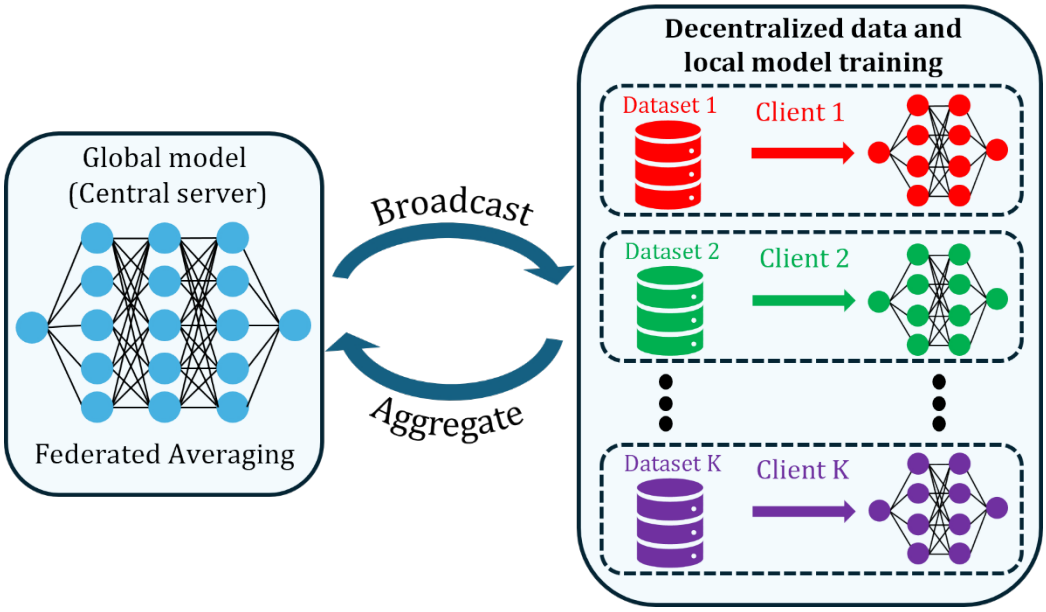


Figure 3. A general overview of federated machine learning. Each client trains a local model on heterogenous dataset, and the models are iteratively aggregated on a central server to obtain a global model without sharing raw data.

From an optimization perspective, federated learning can be formulated as the minimization of a global objective function constructed from a weighted combination of local client losses (Zhang et al., 2025). Let $\mathbf{W}$ denote the trainable weights of a neural-network model shared across all clients. The global objective function is defined as

$$\min_{\mathbf{W}} \mathcal{L}_{Fed}(\mathbf{W}) = \sum_{k=1}^{K} \frac{N_k}{N} \mathcal{L}_k(\mathbf{W}), \quad N = \sum_{k=1}^{K} N_k \tag{34}$$

where K is the total number of clients, N_k is the number of data points at the k-th client and $\mathcal{L}_k$ is the local loss function for client k defined as

$$\mathcal{L}_k(\mathbf{W}) = \frac{1}{N_k}\sum_{i=1}^{N_k} \ell\left(\hat{y}_i^{(k)}, \hat{y}_{i,exp}^{(k)}\right) \tag{35}$$

where $\hat{y}_i^{(k)}$ and $y_{i,\mathrm{exp}}^{(k)}$ denote the predicted and experimental responses of the i-th data point at client k, respectively, and $\ell(\,)$ is a sample-wise loss function.

Subsequently, the classical federated averaging algorithm proceeds through repeated communication rounds (McMahan et al., 2017). At communication round r, the server broadcasts the current global weights $\mathbf{W}^{\mathrm{r}}$ to all clients. Each client initializes its local model as $W_k^{r,0} = \mathbf{W}^r$. Starting with this initialization, each client performs Elocal optimization steps using only its own dataset. For the i-th local step, the gradient of the local loss is computed as

$$g_k^i = \nabla_{\mathbf{W}} L_k(\mathbf{W}_k^{r,i-1}), \qquad i = 1, \dots, E \tag{36}$$

Using a local learning rate η_c, the local weights may be updated by gradient descent as

$$\mathbf{W}_k^{r,i} = \mathbf{W}_k^{r,i-1} - \eta_c g_k^{r,i}, \qquad i = 1, \dots, E \tag{37}$$

After completing the local training stage, each client sends its updated model weights $\mathbf{W}_k^{r,E}$ to the server. The server then constructs the next global model by weighted averaging,

$$\mathbf{W}^{r+1} = \sum_{k=1}^{K} \frac{N_k}{N} \mathbf{W}_k^{r,E} \tag{38}$$

This update gives larger contribution to clients with larger local datasets and corresponds to the standard FedAvg aggregation rule. The cumulative update produced by client k during round r is given as $\Delta\mathbf{W}_k^r = \mathbf{W}_k^{r,E} - \mathbf{W}^r$. The server-side aggregated increment is then

$$\Delta\mathbf{W}^r = \sum_{k=1}^{K} \frac{N_k}{N} \Delta\mathbf{W}_k^r \tag{39}$$

and the global model is updated as

$$\mathbf{W}^{r+1} = \mathbf{W}^r + \Delta\mathbf{W}^r \tag{40}$$

Equations (38) and (40) are two equivalent forms of the federated averaging update.

A more general formulation of federated optimization introduces separate optimization rules at the client and server levels, commonly referred to as Client-OPT and Server-OPT (Reddi et al., 2020). In this setting, the local client update is written as

$$\mathbf{W}_k^{r,i+1} = \mathrm{ClientOPT}(\mathbf{W}_k^{r,i}, g_k^{r,i+1}, \eta_c, r), \qquad i = 0, \dots, E-1 \tag{41}$$

After E local steps, the client-side model change is

$$\Delta\mathbf{W}_k^r = \mathbf{W}_k^{r,E} - \mathbf{W}_k^{r,0} \tag{42}$$

The server aggregates the client updates as

$$\Delta \mathbf{W}^r = \sum_{k=1}^{K} \frac{N_k}{N} \Delta \mathbf{W}_k^r \tag{43}$$

and finally, it updates the global model according to

$$\mathbf{W}^{r+1} = \text{ServerOPT}(\mathbf{W}^r, -\Delta \mathbf{W}^r, \eta_s, r) \tag{44}$$

where η_s is the server learning rate. Within this generalized framework, standard FedAvg is recovered as a special case in which the clients perform local gradient-based optimization and the server applies weighted averaging of the resulting local models.

3.2. I-FedSciML Framework for Identifying SGP Model Parameters

The SGP model with a varying length scale introduced in Section 2 is governed by a set of parameters that control the microscale material response. Accurate identification of these parameters is essential for capturing size-dependent behavior in geometrically distinct micro-scale experiments. In this regard, we propose that the parameter identification problem is formulated within the federated scientific machine learning framework described in the previous section.

The main objective is to infer the SGP parameter sets from multiple experimental datasets associated with different specimen geometries and loading configurations. Since the observed micro-scale response is strongly influenced by geometric scale, each experimental curve will be treated as an independent federated client. Accordingly, the local dataset of each client corresponds to one test configuration, characterized by its own geometric descriptors and measured response data. Hence, the shared model will learn a global mapping between the geometric descriptors and the corresponding SGP model parameters, while each client retains its own experimental data locally.

The framework defines clients associated with different geometric configurations (d_k, D_k, h_k), where d_k denotes the grain size, D_k denotes the specimen-scale macroscopic characteristic size, and h_k denotes the beam thickness. For each client k, the available experimental dataset is written as

$$\mathcal{D}_k = \left\{ \left(\varepsilon_{s,i}^{(k)}, M_{i,exp}^{(k)} \right) \right\}_{i=1}^{N_k} \tag{45}$$

where ε_s is the imposed strain measure and M_{exp} is the experimentally measured bending moment or torsion. These datasets are explicitly assigned to independent clients with distinct (d, D, h) values and corresponding experimental moment/torsion–strain points. To account for the scale difference between geometric quantities, the geometry is first transformed using logarithmic normalization:

$$\boldsymbol{z}_k = \frac{[\log_{10}(d_k), \log_{10}(D_k), \log_{10}(h_k)]^T - \mu_z}{\sigma_z}, \tag{46}$$

where μ_z and σ_z are computed from the geometries of all available clients. The inverse model is represented by a neural network with shared trainable weights $\mathbf{W}$. For each client, the

network receives the normalized geometry vector $\boldsymbol{z}_k$ and predicts the corresponding SGP parameter vector:

$$\boldsymbol{\theta}_k = \mathcal{N}_{\mathbf{W}}(\boldsymbol{z}_k) = \begin{bmatrix} \sigma_{\text{ref}}^{(k)} \\ \sigma_0^{(k)} \\ m^{(k)} \end{bmatrix} \tag{47}$$

Here, $\sigma_{\text{ref}}^{(k)}$, $\sigma_0^{(k)}$, and $m^{(k)}$ are the client-specific model parameters identified for the k-th experimental curve. The neural network therefore acts as a geometry-conditioned inverse operator which maps the geometry features to the SGP parameters.

To ensure physically admissible parameter values during training i.e., $\theta_j^{\min} \le \theta_j \le \theta_j^{\max}$, each network output is passed through a bounded sigmoid transformation. If $r_j^{(k)}$ is the raw neural-network output associated with parameter $\theta_j^{(k)}$, then the bounded parameter is computed as

$$\theta_j^{(k)} = \theta_{j,\min} + \left(\theta_{j,\max} - \theta_{j,\min}\right)\text{sigmoid}\left(r_j^{(k)}\right). \tag{48}$$

For each client, the predicted parameter vector $\boldsymbol{\theta}_k$ is inserted into a differentiable SGP model. The forward model evaluates the bending moment/torsion as

$$M^{(k)} = \mathcal{F}_{SGP}\left(\varepsilon_s^{(k)}, h_k, D_k, d_k; \boldsymbol{\theta}_k\right), \tag{49}$$

where $\mathcal{F}_{\text{SGP}}$ denotes the SGP operator. The length-scale relation is then used in the forward model. Subsequently, the bending or torsional response is then evaluated through numerical thickness integration. The integral is evaluated numerically using a dense grid over $y \in [10^{-8}, 0.5]$, and all operations are implemented in PyTorch so that gradients can be backpropagated through the SGP forward model.

For client k, the local inverse problem is expressed as the minimization of the discrepancy between the predicted and measured bending moments/torsion. The loss function is defined using a relative mean-squared error as follows

$$\mathcal{L}_k(\boldsymbol{W}) = \frac{1}{N_k}\sum_{i=1}^{N_k}\left[\frac{M^{(k)}\left(\varepsilon_{s,i}^{(k)}; \mathcal{N}_{\boldsymbol{W}}(\boldsymbol{z}_k)\right) - M_{i,exp}^{(k)}}{M_{i,exp}^{(k)}}\right]^2 \tag{50}$$

Subsequently the federated learning procedure explained in previous section is initiated where global objective is implemented as a weighted aggregation of all local client objectives. Following the federated-learning principle of collaborative parameter identification, neural-network weights **W** are communicated and averaged. The resulting framework therefore identifies a distinct parameter set

$$\boldsymbol{\theta}_k^* = \left[\sigma_{\text{ref}}^{(k)*}, \sigma_0^{(k)*}, m^{(k)*}\right]^T \tag{51}$$

for each experimental curve, while preserving a shared global representation of the geometry–parameter relationship. This is a key distinction from conventional independent inverse calibration. In independent calibration, each curve is fitted separately, and no information is transferred between geometrically different experiments. In contrast, the

present I-FedSciML formulation allows all experimental curves to contribute to a common inverse mapping, while still producing client-specific SGP parameters through the geometry-conditioned input. The overall schematic workflow of the I-FedSciML is illustrated in Figure 4. We demonstrate the effectiveness of I-FedSciML framework for identifying the SGP model parameters using the micro-bending and micro-torsion experiments of thin beams and wires.

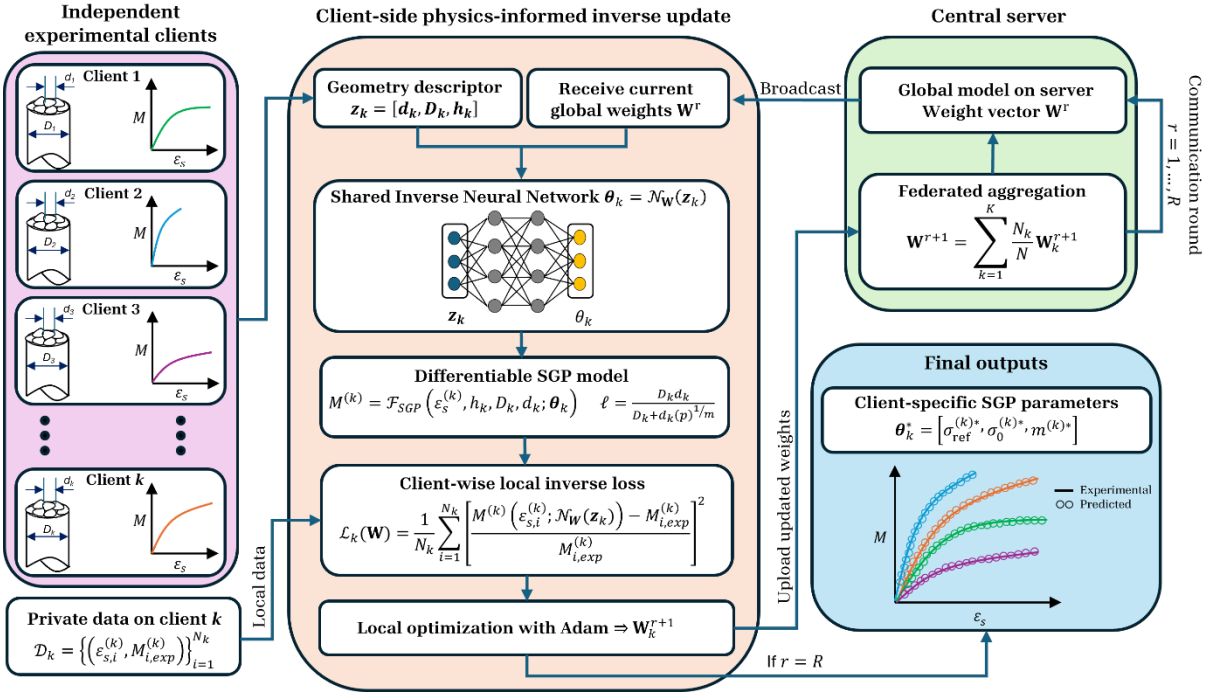


Figure 4. The schematic workflow of I-FedSciML framework for client-specific parameter identification of micro/nano structures

4. Results of I-FedSciML Parameter Identification

In this section evaluates the performance of the inverse I-FedSciML framework developed in Section 3 for identifying SGP model parameters from three micro-bending experiments and one micro-torsion test on thin wires. The I-FedSciML simulations were implemented using the PyTorch library and executed on a high-performance workstation equipped with a 12th Gen Intel® Core™ i9-12900H processor operating at 2.5 GHz and 64 GB of RAM. To ensure reproducibility and enable fair comparisons among different simulations, a fixed random seed of 20260401 was used throughout the training process. The shared inverse model is a fully connected neural network that contains three hidden layers, each with 64 neurons, and uses the SiLU activation function. During federated training, each client performs local optimization using the Adam optimizer with a learning rate of 10^{-3}. The final simulations were conducted for 150 communication rounds, with 80 local epochs per client in each round and a batch size of 32. Gradient clipping with a maximum norm of 1.0 was applied during local training to improve numerical stability. Model performance and parameter evolution were recorded throughout training, including mean training loss, RMSE, MAPE, R^2.

4.1. Micro-Bending of Thin Annealed Nickel Foils

Stölken and Evans (1998) performed micro-bending experiments on thin annealed nickel foils with different specimen thicknesses to characterize size-dependent plastic deformation at the microscale. In the present study, three experimental bending curves are considered, corresponding to specimens with characteristic macroscopic sizes $D = 12.5$, 25, and 50 μm, and grain sizes $d = 31$, 77, and 103 μm, respectively. The experimental responses are interpreted using the generalized SGP model of Voyiadjis and Abu Al-Rub (2005), in which the material length scale is expressed as a physically motivated function of the microstructural features of the material. The constitutive response is governed by three unknown SGP parameters including reference stress (σ_{ref}), hardening modulus (σ_0), and the hardening exponent (m). Our objective is to identify these parameters by fitting the experimentally measured normalized bending moment (M/bh^2) vs. normalized surface curvature ($\kappa h/2$).

Here each experimental bending curve in I-FedSciML framework is treated as an independent client. Accordingly, three clients are defined such that Client 1 corresponds to $(d, D) = (31, 12.5)$ μm, Client 2 to $(d, D) = (77, 25)$ μm, and Client 3 to $(d, D) = (103, 50)$ μm. The initial parameter values were set to $\sigma_{\text{ref}} = 80$ (MPa), $\sigma_0 = 1000$ (MPa), and $m = 1$. To ensure physically admissible solutions during optimization, the parameters were constrained within the bounds $10 \leq \sigma_{\text{ref}} \leq 400$, $100 \leq \sigma_0 \leq 5000$, and $0.2 \leq m \leq 5$, respectively.

The evolution of the SGP parameters illustrated in Figure 5 indicates that the I-FedSciML framework reaches a relatively stable client-specific parameterization after the initial transient communication rounds. It can be seen that σ_{ref} rapidly decreases for all three clients during the early rounds, followed by convergence toward nearly the same lower-bound value. In contrast, σ_0 exhibits clear client-dependent behavior where Client 1 converges to the highest hardening modulus, whereas Clients 2 and 3 stabilize at lower values. The hardening exponent m also exhibits client-specific variation but the identified values remain relatively close to one another, ranging from 0.75 to 0.88.

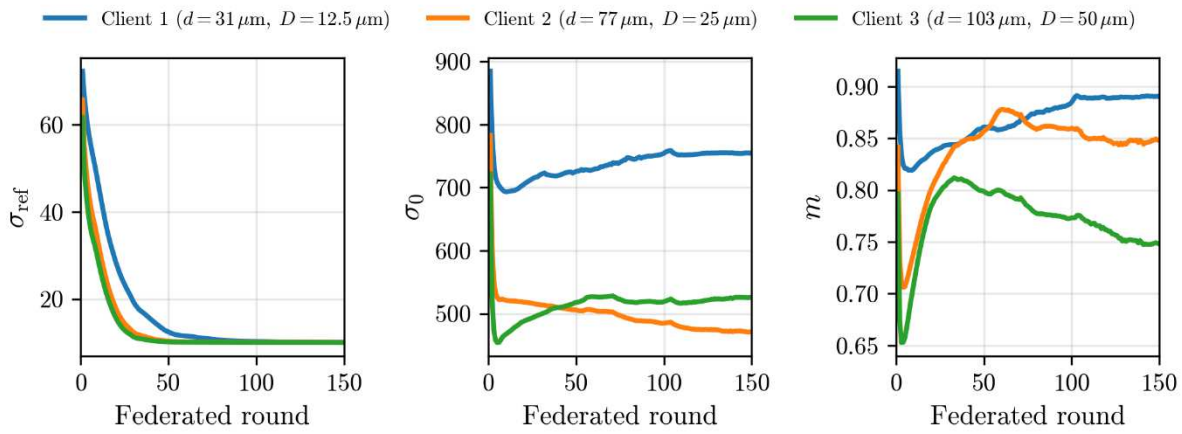


Figure 5. Evolution of geometry-conditioned SGP parameters ($\sigma_{ref}, \sigma_0, m$) for three different clients during federated communication rounds

The identified SGP parameter values for the three experiments are summarized in Table 1. The results show that the inverse I-FedSciML framework successfully provides distinct client-specific parameter sets while satisfying the prescribed physical bounds. For all clients, σ_{ref} converges to nearly the same value (close to 10 MPa), suggesting that this parameter has limited influence in distinguishing the three bending responses in the present inverse setting. In contrast, σ_0 exhibits more pronounced variation among the clients, indicating that the hardening modulus plays a more dominant role in adapting the SGP response to each experimental curve. The m also shows slight client-dependent variation, reflecting moderate geometry-dependent differences in the inferred hardening behavior.

Table 1. Identified SGP model parameters for the three micro-bending clients using the I-FedSciML framework

Parameters	**Bounds**	**Initial guess**	**Identified optimal values**		
			Client 1	**Client 2**	**Client 3**
$\boldsymbol{\sigma_{ref}}$ **[MPa]**	10 - 400	80	10.06	10.01	10.00
$\boldsymbol{\sigma_0}$ **[MPa]**	100 - 5000	1000	754.91	471.17	525.83
$\boldsymbol{m}$	0.2 - 5	1	0.88	0.85	0.75

The comparison in Figure 6 shows that the client-specific parameters identified by the inverse I-FedSciML framework reproduce the experimental micro-bending responses with good overall accuracy. For all three clients, the predicted normalized moment–curvature curves closely follow the corresponding experimental trends, capturing both the monotonic increase of $M/(bh^2)$ with ε_s and the separation between the three size-dependent responses. The smallest characteristic thickness associated with Client 1 exhibits the highest normalized bending moment, while Clients 2 and 3 show progressively lower responses, consistent with the expected size effect.

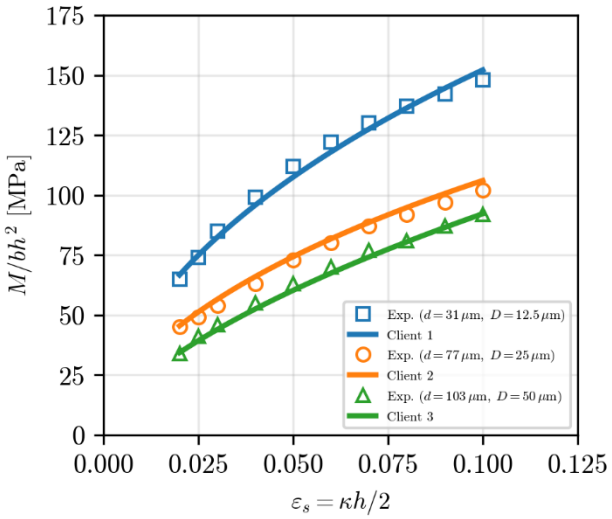


Figure 6. Comparison of experimental and I-FedSciML-predicted micro-bending moment–curvature responses using client-specific SGP parameters

The quantitative error metrics provided in Table 2 confirm the strong predictive performance of the inverse I-FedSciML framework for all three clients. The RMSE values remain low, ranging from 1.885 to 2.939, while the MAE values vary between 1.577 and 2.658. This indicates small absolute deviations between the experimental and predicted bending responses. The MAPE values are also limited, remaining close to 2.4–3.1%, which shows that the relative prediction errors are small across all datasets. Furthermore, the high R^2 values, between 0.982 and 0.990, demonstrate that the identified client-specific SGP parameters accurately capture the experimental trends.

Table 2. Quantitative error metrics for micro-bending responses predicted using client-specific SGP parameters

Metrics	**Client 1**	**Client 2**	**Client 3**
MSE	8.628	6.564	3.554
RMSE	2.939	2.562	1.885
MAE	2.658	2.341	1.577
MAPE	2.427	3.104	2.695
R^2	0.989	0.982	0.990

Figure 7 illustrates the evolution of the Clients' mean local training loss at different federated rounds. The relative MSE loss decreases sharply from 0.00175 during the first few rounds, indicating that the shared inverse model quickly learns an effective mapping from the client descriptors to the SGP parameters. After this initial transient phase, the loss continues to decrease more gradually and reaches a nearly constant value of approximately 0.0004 after 50 rounds. This plateau suggests that the federated training process has converged and that additional communication rounds provide marginal improvement.

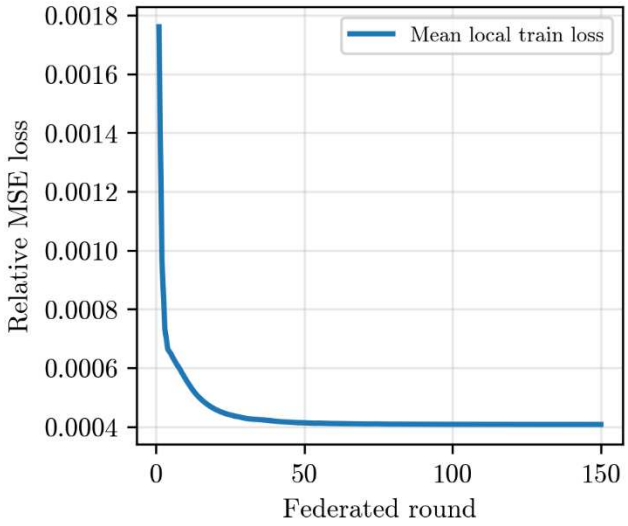


Figure 7. Convergence history of the I-FedSciML framework during federated training.

The round-wise comparison in Figure 8 illustrates how the I-FedSciML framework progressively improves the client-specific SGP predictions during federated training. At Round 1, the predicted curves are still poorly calibrated, particularly for Clients 2 and 3, where the responses are overestimated over most of the strain range. By Round 50, the three predictions become noticeably closer and match the slope of the experimental curves more consistently. At the final Round 150, the predictions show good agreement with the experimental measurements for all three clients, capturing the increasing normalized moment with $\varepsilon_s = \kappa h/2$ as well as the size-dependent separation among the datasets. The improvement from Round 1 to Round 150 demonstrates that the shared inverse model benefits from iterative FedAvg communication while still producing distinct client-specific responses.

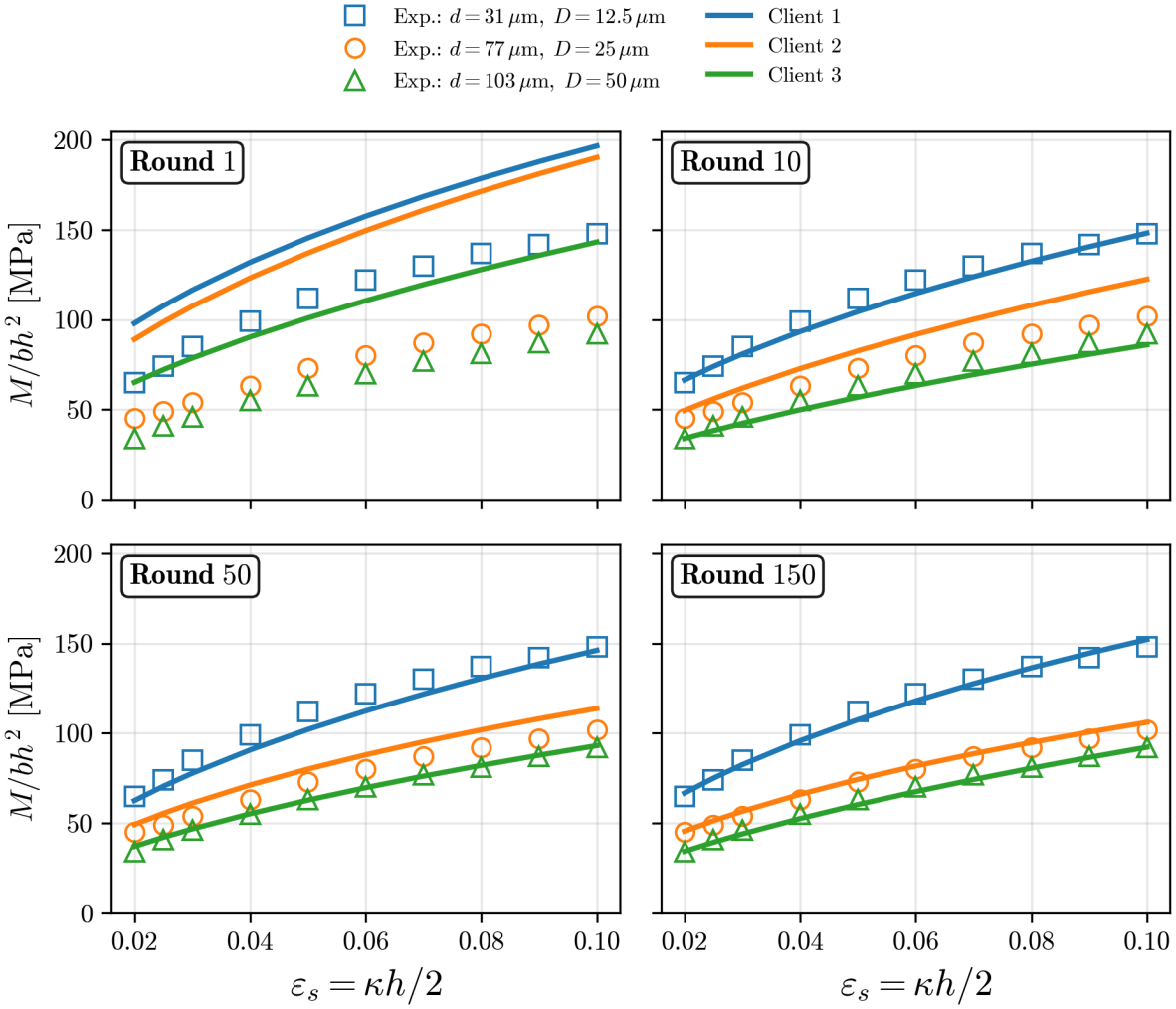


Figure 8. Comparison of experimental moment–curvature data of annealed Nickel foils with SGP predictions obtained at selected federated communication rounds (1, 10, 50, 150).

4.2. Micro-Bending of Thin LIGA Nickel Foils

Shrotriya et al. (2003) performed micro-bending experiments on thin polycrystalline LIGA nickel foils. In the present study, four experimental bending curves are considered,

corresponding to specimens with characteristic sizes $D = 25, 50, 100$, and $200\ \mu$m, and grain sizes $d = 0.5,\ 0.79,\ 1.26$, and $1.37\ \mu$m, respectively. As in Section 4.1, the constitutive response is described using the SGP model, in which the unknown parameters σ_{ref}, σ_0, and m must be identified by fitting the experimentally measured moment–curvature response. To this end, the proposed I-FedSciML framework treats each experimental bending curve as an independent federated client. Accordingly, four clients are defined as Client 1 ($d = 0.5, D = 25$), Client 2 ($d = 0.79, D = 50$), Client 3 ($d = 1.26, D = 100$) and Client 4 ($d = 1.37, D = 200$). For consistency with the previous subsection, the same initial parameter values and admissible bounds are used for the inverse identification process.

The evolution of the identified SGP parameters in Figure 9 shows that the I-FedSciML framework develops client-specific parameter trajectories during the communication rounds. Unlike the previous micro-bending case, σ_{ref} separates significantly among clients, with Client 1 reaching the highest value and Client 4 decreasing toward the lowest value by the final round. This indicates that the reference stress contributes more strongly to distinguishing the LIGA nickel bending responses. The hardening modulus σ_0 also exhibits pronounced client-dependent evolution, especially after approximately 100 rounds. The hardening exponent m generally decreases with increasing communication rounds for all clients. This suggests that optimization compensates for the increasing stress-scale parameters by reducing the hardening nonlinearity. Overall, a pronounced coupling among σ_{ref}, σ_0, and m during the federated training process is evident from this figure.

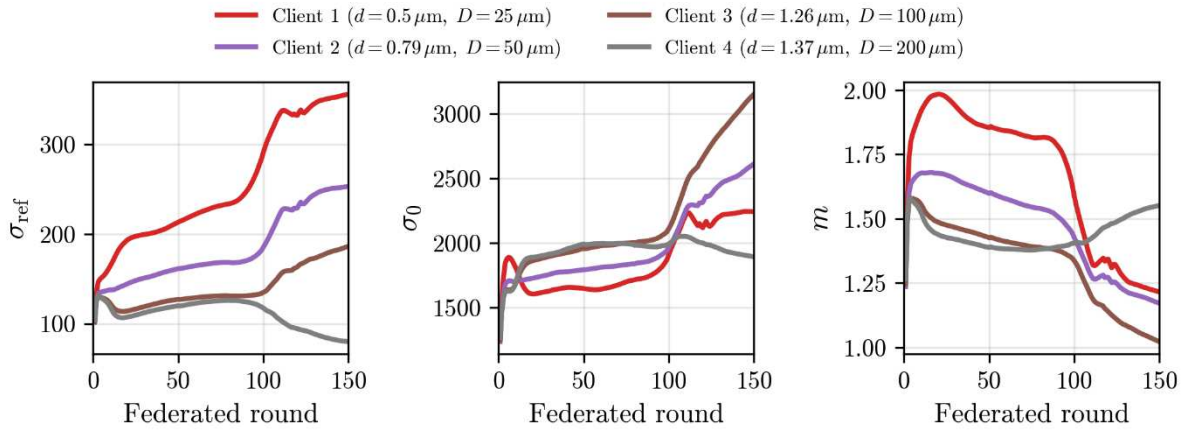


Figure 9. Evolution of identified SGP parameters for LIGA nickel micro-bending clients during federated training

The optimal parameters identified for the LIGA nickel micro-bending datasets at the end of I-FedSciML are presented in Table 3. The σ_{ref} decreases systematically from Client 1 (355.6 MPa) to Client 4 (80.1 MPa), indicating that this parameter plays an important role in differentiating the bending responses for the different geometrical configurations. In contrast, the σ_0 remains relatively high for all clients, with the largest value obtained for Client 3 (3151.8 MPa). The m varies moderately between 1.02 and 1.55. The table also confirms that the I-FedSciML framework successfully identifies all parameters within their prescribed physical bounds.

Table 3. Identified SGP model parameters for LIGA nickel micro-bending clients using the I-FedSciML framework

Parameters	Bounds	Initial guess	Identified optimal values			
			Client 1	Client 2	Client 3	Client 4
σ_{ref} [MPa]	10 - 400	80	355.6	252.8	186.2	80.1
σ_0 [MPa]	100 - 5000	1000	2240.7	2611.4	3151.8	1891.8
m	0.2 - 5	1	1.21	1.17	1.02	1.55

The comparison between the experimental data and the I-FedSciML-predicted responses in Figure 10 shows good agreement for all four micro-bending clients. The identified SGP parameters successfully reproduce the increasing trend of the normalized bending moment with the normalized surface curvature. Minor deviations are observed at some data points, but the overall slopes and magnitudes of the experimental curves are well represented.

Statistical metrics quantifying the error calculated between experiments and I-FedSciML-predicted responses for all four clients are provided in Table 4. The RMSE values remain relatively low, ranging from 2.65 to 4.29, while the MAE values vary between 2.34 and 3.85. Similarly, the MAPE values are also small, remaining below 3.5% for all clients. This demonstrates good relative accuracy across the different geometric configurations. On the other hand, the high R^2 values ranging between 0.925 and 0.974, further confirm that the predicted SGP responses capture the experimental trends. Client 4 shows the lowest R^2 and the highest MAPE, indicating a slightly larger prediction discrepancy compared with the other clients; nevertheless, the overall agreement remains satisfactory.

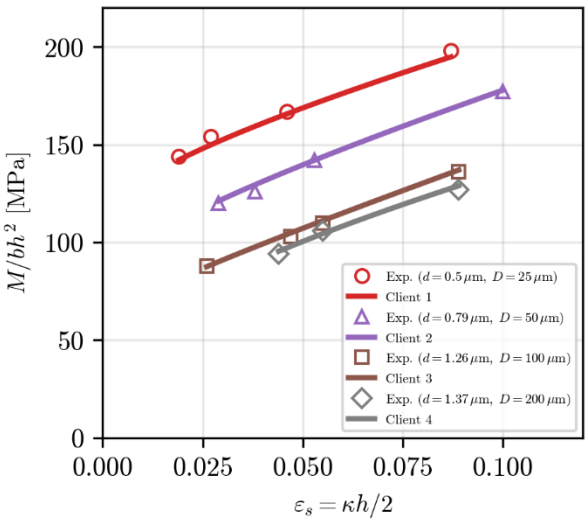


Figure 10. Comparison of experimental and I-FedSciML-predicted moment–curvature for LIGA nickel micro-bending clients

Table 4. Quantitative error metrics for SGP responses of LIGA nickel micro-bending clients

Metrics	Client 1	Client 2	Client 3	Client 4
MSE	18.48	12.72	7.06	13.44

RMSE	4.29	3.56	2.65	3.66
MAE	3.85	2.65	2.34	3.65
MAPE	2.31	1.98	2.11	3.40
R^2	0.956	0.973	0.974	0.925

The convergence history presented in Figure 11 demonstrates a consistent reduction in the mean local relative MSE loss throughout the federated training process. Starting from an initial value of approximately 9.0×10^{-4}, the loss drops sharply within the first few communication rounds, indicating rapid adjustment of the shared inverse model to the local LIGA nickel datasets. After this initial reduction, the loss decreases more gradually and remains nearly stable until around 90–100 rounds, where a second noticeable improvement occurs. By the final round, the loss reaches approximately 3.9×10^{-4}. The learning behavior demonstrates the continued refinement of the geometry-conditioned parameter mapping.

Subsequently, the round-wise comparison in Figure 12 demonstrates the progressive improvement of the I-FedSciML-predicted SGP responses. At Round 1, the predicted curves substantially underestimate the experimental responses for all clients, indicating that the initial shared inverse model has not yet learned the appropriate geometry-dependent parameter mapping. By Round 50, the slopes and magnitudes of the predicted moment–curvature curves become more consistent with the experimental trends. At the final Round 150, the predicted responses show good agreement with the measured data for all clients, capturing both the monotonic increase of moment with curvature and the size-dependent ordering of the LIGA nickel specimens.

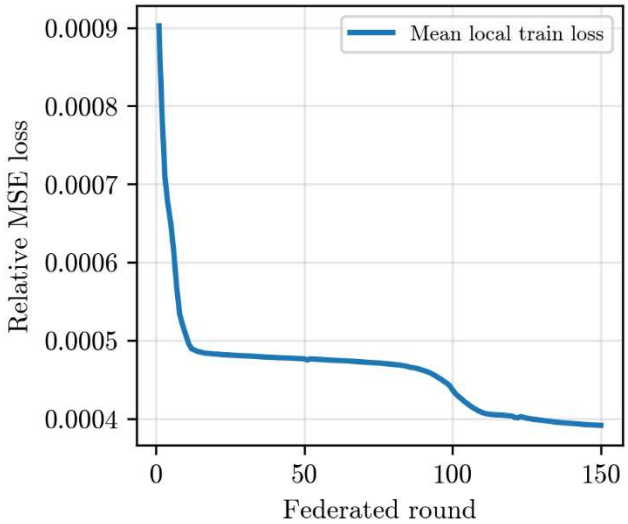


Figure 11. Convergence history of the I-FedSciML framework for LIGA nickel

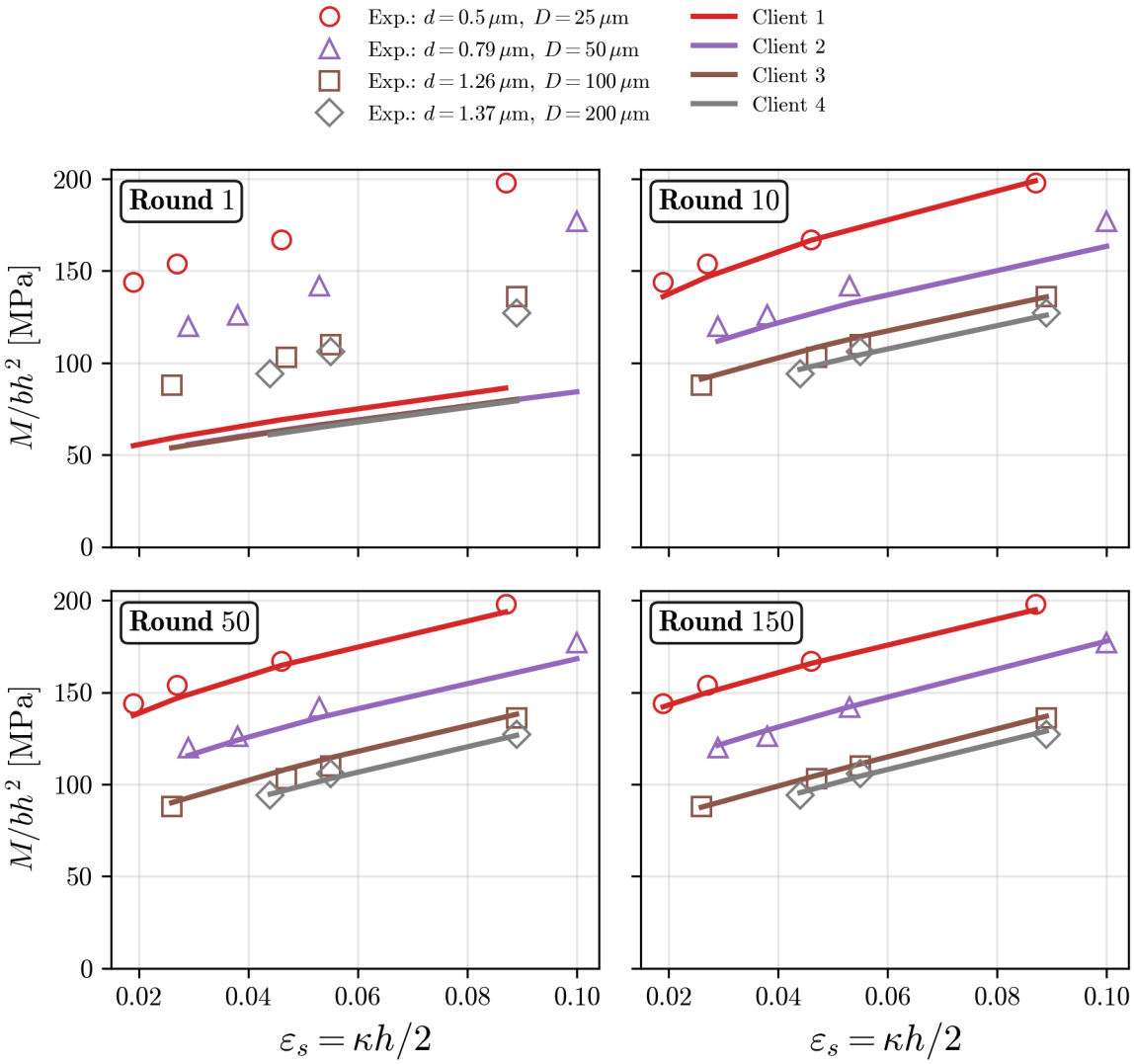


Figure 12. Evolution of SGP predictions for LIGA nickel micro-bending clients at selected federated communication rounds (1, 10, 50, and 150)

4.3. Micro-Bending of Thin Aluminum Beams

Haque and Saif (2003) conducted micro-bending experiments on thin aluminum beams to examine size-dependent plastic behavior at small length scales. In this study, two experimental bending curves are considered, corresponding to specimens with characteristic sizes $D = 0.1$ and $0.2\ \mu$m and grain sizes $d = 0.05$ and $0.1\ \mu$m, respectively. As in the previous cases, the SGP model parameters σ_{ref}, σ_0, and m are identified by fitting the measured moment–curvature response. Each experimental curve is treated as an independent client within the I-FedSciML framework, with Client 1 ($d = 0.05, D = 0.1$) and Client 2 ($d = 0.1, D = 0.2$). The same initial parameter values and admissible bounds used in the previous subsections are adopted for consistency.

The parameter evolution in Figure 13 indicates that the I-FedSciML framework rapidly stabilizes the identified SGP parameters for the two aluminum micro-bending clients. The σ_{ref} decreases sharply within the first few communication rounds and then converges to a nearly constant value for both clients. In contrast, σ_0 shows a strong client-specific separation such that Client 1 rapidly increases and stabilizes near the upper bound, whereas Client 2 converges to a lower but nearly constant value. This indicates that σ_0 plays the dominant role in adapting the SGP response to the two geometries. The m also exhibits different behavior between the clients; Client 2 stabilizes smoothly around 0.782, while Client 1 shows some fluctuations before converging near 0.916. The summary of the identified parameters for the two aluminum micro-bending datasets is provided in Table 5. This table indicates that σ_{ref} has limited and m has moderate influence in differentiating the two experimental responses within the present inverse setting. In contrast, σ_0 plays the dominant role in fitting the aluminum bending behavior.

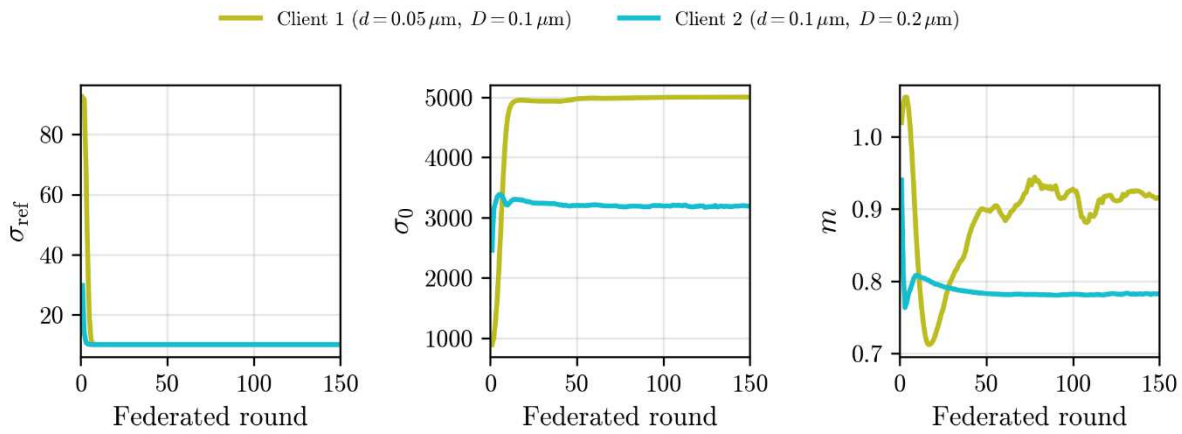


Figure 13. Evolution of identified SGP parameters for aluminum micro-bending clients during federated training

Table 5. Identified parameters for aluminum micro-bending clients using the I-FedSciML framework

Parameters	**Bounds**	**Initial guess**	**Identified optimal values**	
			Client 1	**Client 2**
$\boldsymbol{\sigma_{ref}}$ **[MPa]**	10 - 400	80	10.0	10.0
$\boldsymbol{\sigma_0}$ **[MPa]**	100 - 5000	1000	4999.5	3190.1
$\boldsymbol{m}$	0.2 - 5	1	0.916	0.782

Figure 14 shows that the identified SGP parameters reasonably reproduce the aluminum micro-bending responses for both clients. The predicted moment increases with curvature and captures the clear separation between Client 1 and Client 2, reflecting the geometry-dependent size effect. The agreement is particularly good for Client 2, while Client 1 shows a slight underprediction at higher curvature values. The error metrics in Table 6 indicate that Client 1 has a higher absolute error, with RMSE = 22.5 and MAE = 16.1. Client 2 shows lower absolute errors, with RMSE = 8.3 and MAE = 7.3; however, its MAPE is higher at 10.7%,

indicating a relatively larger percentage deviation due to the lower response magnitude. The R^2 values of 0.898 and 0.904 show that the predicted curves still capture the main experimental trends for both clients.

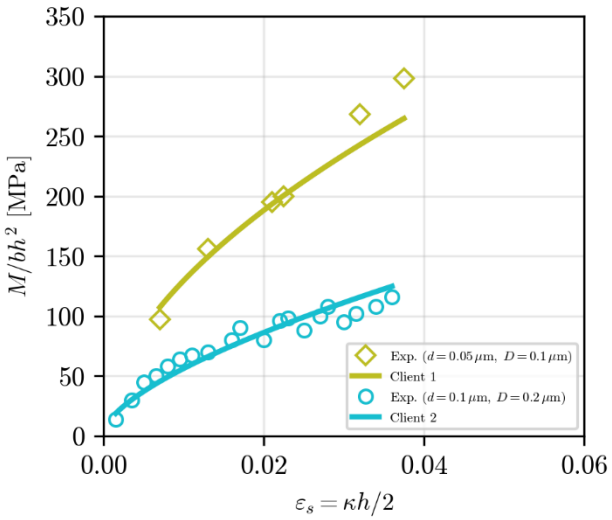


Figure 14. Comparison of experimental and I-FedSciML-predicted responses for aluminum micro-bending clients

Table 6. Quantitative error metrics for predicted SGP responses of aluminum micro-bending clients

Metrics	**Client 1**	**Client 2**
MSE	509.7	70.1
RMSE	22.5	8.3
MAE	16.1	7.3
MAPE	7.3	10.7
R^2	0.898	0.904

The convergence history in Figure 15 shows that the mean local relative MSE loss decreases rapidly during the early federated rounds. The initial loss is approximately 3.5 x 10^{-2} and drops sharply within the first few communication rounds, indicating that the shared inverse model quickly adjusts to the two aluminum micro-bending clients. After this initial reduction, the loss stabilizes at nearly 1.25 x 10^{-2} and remains almost constant until the final round.

Subsequently, the round-wise comparison in Figure 16 highlights the progressive improvement of the I-FedSciML predicted responses for the two aluminum micro-bending clients. At Round 1, the predictions are not yet well calibrated: Client 1 is strongly underestimated, while Client 2 shows partial agreement but still deviates at higher curvature values. By Round 50, the predicted curves move closer to the experimental trends, indicating rapid early adjustment of the shared inverse model. At the final Round 150, the Client 2 predictions closely follow the overall experimental behavior, while Client 1 still shows some underprediction at the highest curvature values. Overall, the figure demonstrates that

federated training progressively improves the reconstruction of the aluminum micro-bending responses over successive communication rounds.

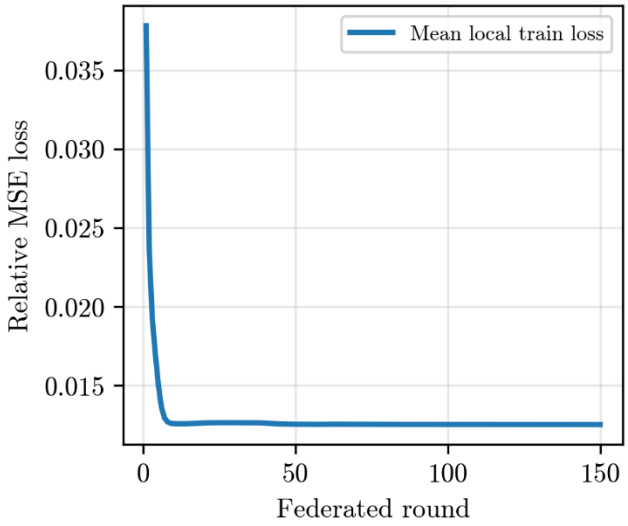


Figure 15. Convergence history of the I-FedSciML framework for aluminum micro-bending clients

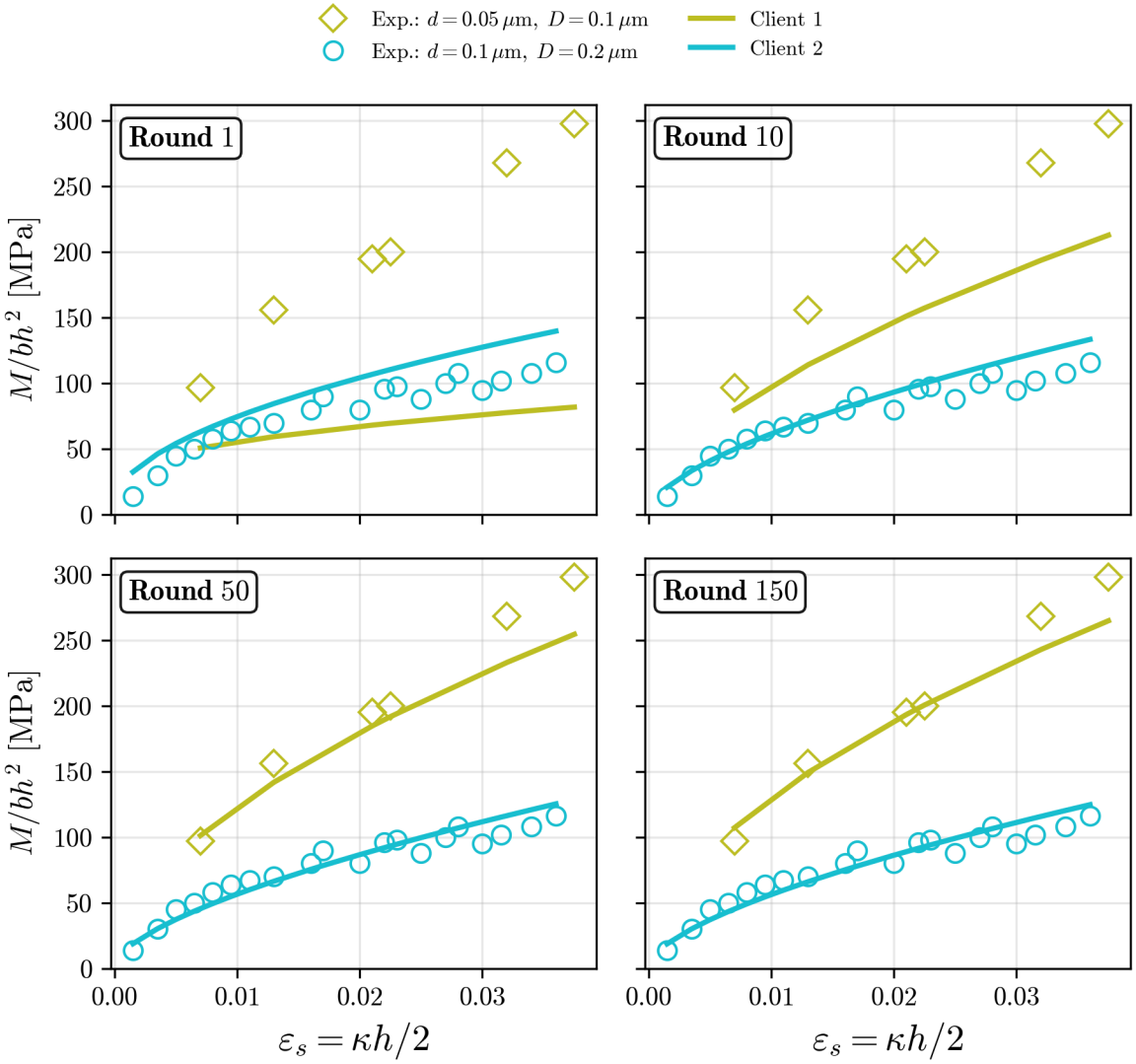


Figure 16. Round-wise evolution of I-FedSciML-predicted SGP responses for aluminum micro-bending clients.

4.4. Micro-Torsion of Thin Copper Wires

Fleck et al. (1994) performed micro-torsion experiments on thin copper wires to examine strain-gradient-induced hardening at small length scales. In the present study, five experimental torsion curves are considered, corresponding to specimens with characteristic sizes D = 12, 15, 20, 30, 170 μm, and grain sizes d = 5, 7, 9, 12, 25 μm, respectively. The SGP model parameters σ_{ref}, σ_0, and m are identified by fitting the experimentally measured torsional response. Each torsion curve is treated as an independent federated client such as Client 1 ($d = 5, D = 12$), Client 2 ($d = 7, D = 15$), Client 3 ($d = 9, D = 20$), Client 4 ($d = 12, D = 30$) and Client 5 ($d = 25, D = 170$). For this case, the initial parameter values are set to $\sigma_{\text{ref}} = 20$, $\sigma_0 = 150$, and $m = 1$, while the same admissible parameter bounds used in the previous subsections are retained for consistency.

The parameter evolution for the copper micro-torsion clients in Figure 17 shows client-dependent behavior during federated training. The σ_{ref} exhibits stronger early fluctuations

before reaching a more stable regime after approximately 60–70 communication rounds. In contrast, σ_0 shows a clear separation among clients, with Client 1 increasing continuously toward the highest value, while Clients 4 and 5 stabilize at much lower levels. The m also evolves distinctly for each client, with Client 1 converging to the largest value, while the remaining clients stabilize in a lower range. Overall, the early oscillations in the subfigures indicate noticeable coupling among σ_{ref}, σ_0, and m during the initial stages of federated optimization.

The identified SGP parameters are summarized in Table 7, highlighting their values within the prescribed bounds. The σ_{ref} varies only moderately, ranging from 35.5 to 47.9 MPa. In contrast, the σ_0 decreases systematically from Client 1 to Client 5, from 494.4 MPa to 160.4 MPa. The m also varies noticeably, with the highest value obtained for Client 1 and lower values for the remaining clients.

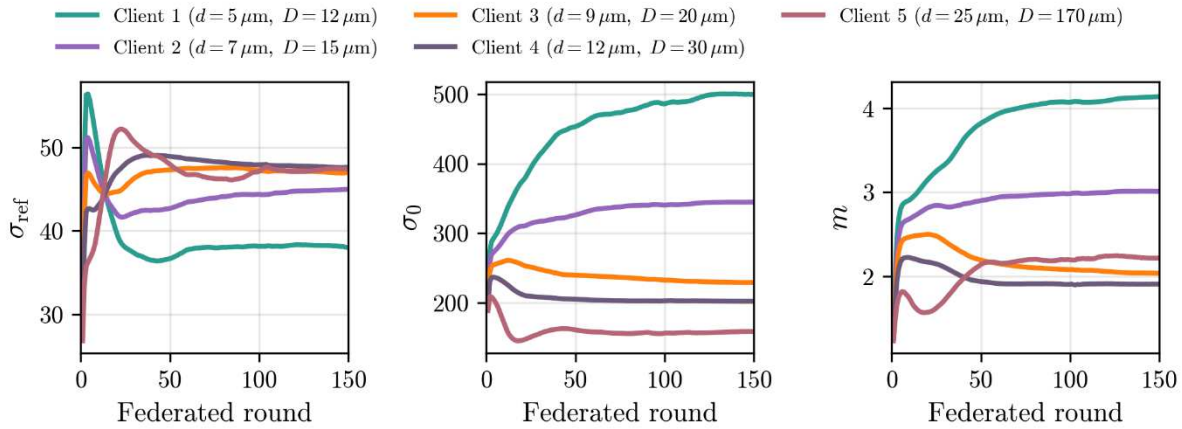


Figure 17. Evolution of SGP parameters for copper micro-torsion clients during federated training

Table 7. Identified model parameters for copper micro-torsion clients using the I-FedSciML

Parameters	Bounds	Initial guess	Identified optimal values				
			Client 1	Client 2	Client 3	Client 4	Client 5
σ_{ref} [MPa]	10 - 400	20	35.5	45.8	46.9	47.9	47.0
σ_0 [MPa]	100 - 5000	150	494.4	349.1	226.8	202.6	160.4
m	0.2 - 5	1	4.1	3.0	3.0	1.9	2.3

Figure 18 shows a strong agreement between the experimental copper micro-torsion data and the identified SGP responses for all five clients. The predicted normalized torque (Q/a^3) increases monotonically with the normalized strain measure ($\varepsilon_s = \kappa a$), and the model successfully captures the separation among the different wire geometries. Client 1 exhibits the highest torsional resistance, followed by Clients 2, 3, 4, and 5, which is consistent with the experimentally observed size-dependent strengthening. The agreement is particularly good over the full deformation range, with the predicted curves closely following both the magnitude and nonlinear trend of the experimental data.

The quantitative error metrics summarized in Table 8 further confirm the accuracy of copper micro-torsion clients' predictions. The RMSE values remain relatively low, ranging from 4.49 to 13.91, while the MAE values range from 3.97 to 12.67 MPa. The MAPE values are also small for all clients, remaining below 3.2%, which demonstrates strong relative accuracy across the different wire geometries. Client 2 exhibits the largest error values, with RMSE = 13.91, MAE = 12.67, and MAPE = 3.13%, but its R^2 value remains high at 0.985, indicating that the overall experimental trend is still well captured.

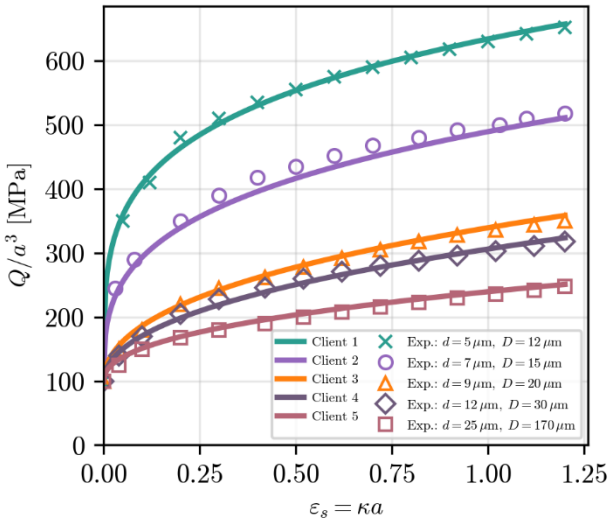


Figure 18. Comparison of experimental and I-FedSciML predicted responses for copper micro-torsion clients

Table 8. Quantitative error metrics for predicted SGP responses of copper micro-torsion clients

Metrics	Client 1	Client 2	Client 3	Client 4	Client 5
MSE	46.81	193.51	20.21	26.31	21.28
RMSE	6.84	13.91	4.49	5.13	4.61
MAE	5.45	12.67	3.97	4.38	4.11
MAPE	1.34	3.13	1.54	1.81	2.19
R^2	0.997	0.985	0.996	0.993	0.988

Figures 19 and 20 collectively demonstrate the convergence behavior and progressive predictive improvement of the I-FedSciML framework for the copper micro-torsion clients. As shown in Figure 19, the mean local relative MSE loss decreases sharply from its initial value (0.165) within the first few communication rounds and then approaches a nearly constant low value. It indicates rapid and stable convergence of the federated training process. This behavior is consistent with the response evolution shown in Figure 20, where the predictions at Round 1 are still poorly calibrated. By Round 10, the predicted curves move closer to the experimental torque–twist data, and further refinement is observed at Rounds 150 and 300. At the final round, the I-FedSciML predicted SGP responses closely reproduce

both the nonlinear trend and the clear size-dependent separation among the five copper wire clients.

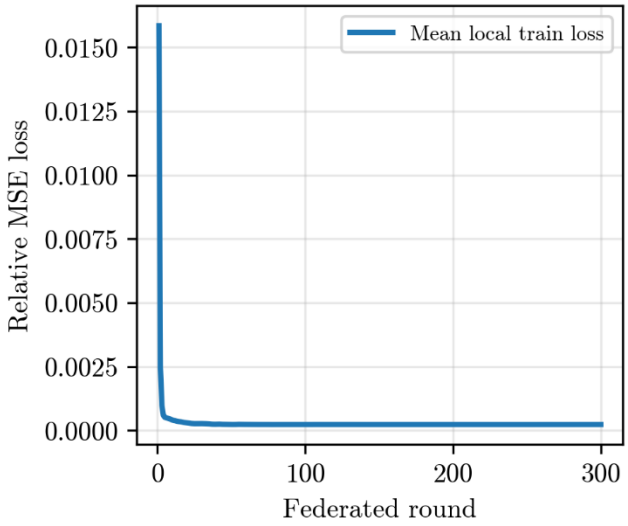


Figure 19. Convergence history of the I-FedSciML for copper micro-torsion clients

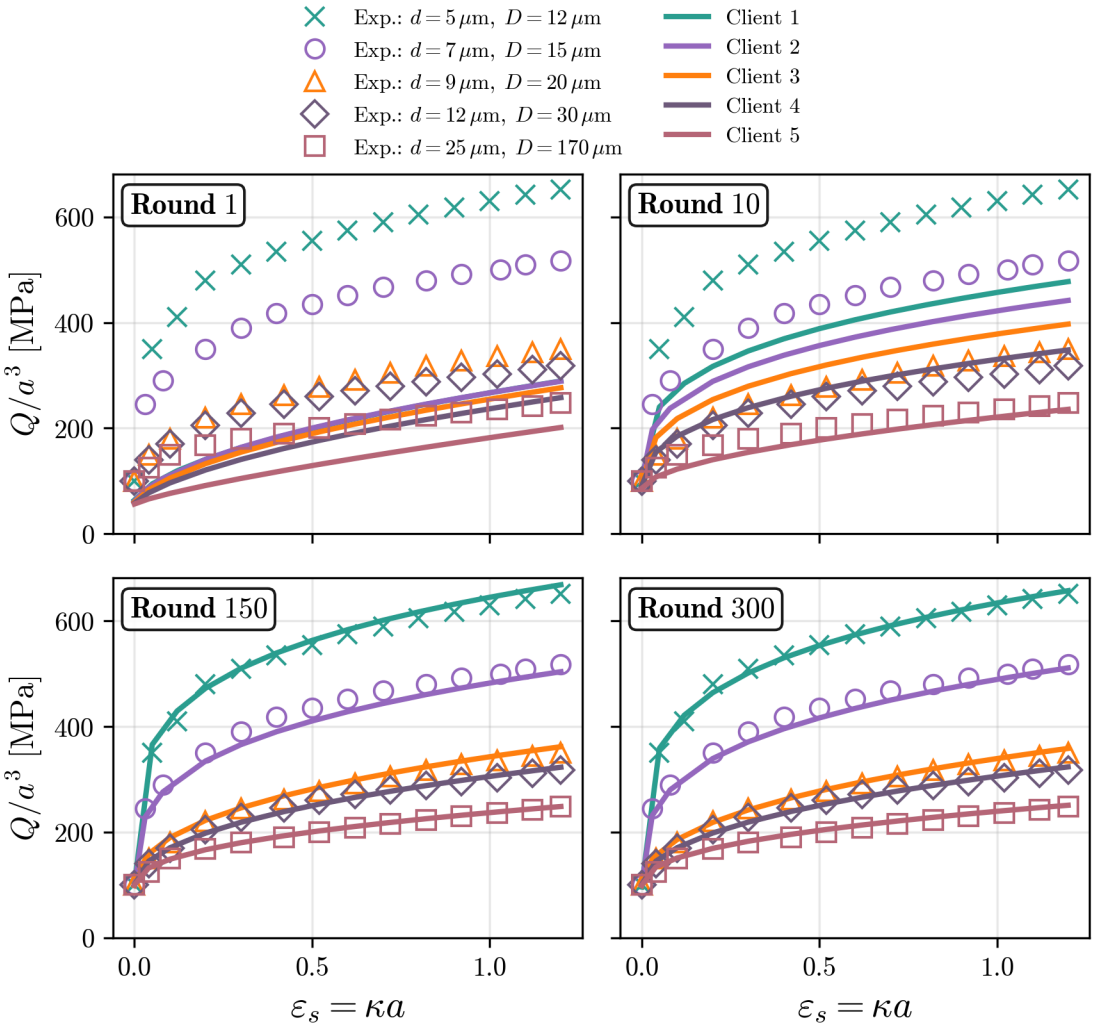


Figure 20. Round-wise evolution of predicted SGP responses for copper micro-torsion clients

4.5. Noise Sensitivity Analysis

To assess the robustness of I-FedSciML framework against measurement uncertainty, synthetic Gaussian noise was introduced into the experimental torsion responses. For each experimental data point, the perturbed response was generated as

$$Q_i^{noise} = Q_i(1 + \eta_i) \tag{51}$$

where Q_i denotes the original experimental value and $\eta_i \sim \mathcal{N}(0, s^2)$ is a zero-mean Gaussian random variable with standard deviation s. We considered four noise levels namely $s =$ 0.010, 0.025, 0.050, 0.10 corresponding to 1%, 2.5%, 5%, and 10% perturbations, respectively. The clean case ($s = 0$) was also evaluated as the reference solution. For each noise level, the federated inverse identification was repeated over $R = 10$ independent noise realizations. The noise sensitivity study is performed for 150 federated communication rounds for computational efficiency.

For each client k, parameter $p \in \{\sigma_{ref}, \sigma_0, m\}$, noise level s, and independent noise realization $r = 1, \dots, R$, the identified parameter is denoted by $p_{k,r}^{(s)}$. The corresponding noise-free federated estimate is denoted by $p_{k,r}^{(0)}$. The mean parameter estimate over the repeated noisy realizations is calculated as

$$\bar{p}_k^{(s)} = \frac{1}{R}\sum_{r=1}^{R} p_{k,r}^{(s)} \tag{52}$$

To compare parameters with different magnitudes, the relative parameter bias induced by measurement noise is evaluated with respect to the corresponding noise-free federated solution as follows,

$$\mathrm{Bias}_{p,k}^{(s),\%} = \frac{100}{R}\sum_{r=1}^{R} \frac{p_{k,r}^{(s)} - p_{k,r}^{(0)}}{\left|p_{k,r}^{(0)}\right|} \tag{53}$$

The variability of the identified parameter across the independent noise realizations is quantified by its sample standard deviation,

$$\mathrm{SDV}_{p,k}^{(s)} = \sqrt{\frac{1}{R-1}\sum_{r=1}^{R}\left(p_{k,r}^{(s)} - \bar{p}_k^{(s)}\right)^2} \tag{54}$$

Accordingly, a small bias indicates that the identified parameter remains close to its noise-free value, whereas a small standard deviation indicates low sensitivity to the particular realization of measurement noise.

As illustrated in Figure 21, the relative parameter bias increases systematically with the imposed noise level for all five clients. The bias in σ_{ref} is the most client-dependent, with Client 1 reaching nearly 18% at 10% noise, while Client 5 remains below about 7%. The bias in σ_0 is comparatively smaller, generally remaining below 6% for Clients 1–4, although Client 5 increases to about 9% at the highest noise level. The hardening exponent m is also sensitive to noise, with relative bias rising to approximately 10%-18% at 10% noise across the clients.

Figure 22 further shows that the uncertainty of the identified parameters increases monotonically with noise level. The mean standard deviation of σ_{ref} grows from below 1 MPa in the clean case to about 5 MPa at 10% noise, while σ_0 increases from roughly 3 MPa to nearly 17 MPa. The standard deviation of m also rises from approximately 0.07 to about 0.40. Overall, these figures show t hat the proposed framework remains stable under low-to-moderate noise, but parameter uncertainty and bias become more pronounced at 10% noise, especially for σ_{ref} and m.

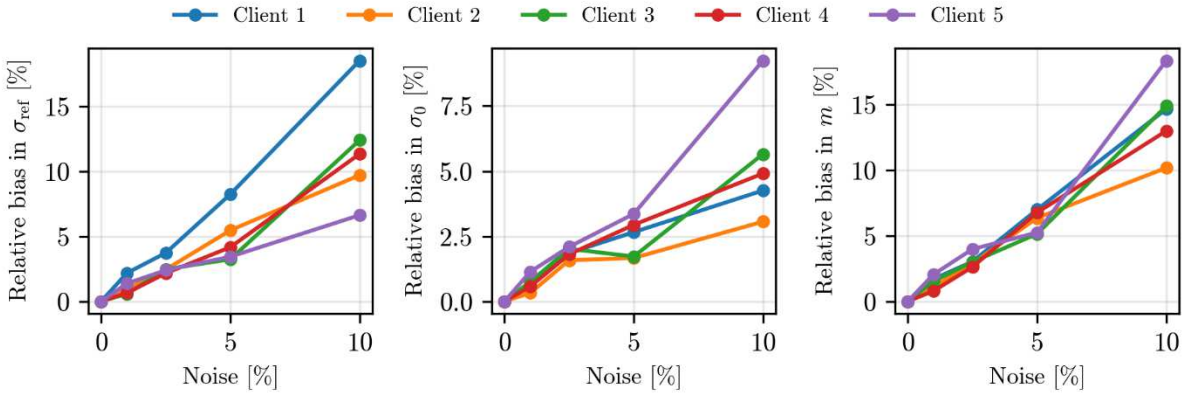


Figure 21. Relative bias of identified SGP parameters under different noise levels

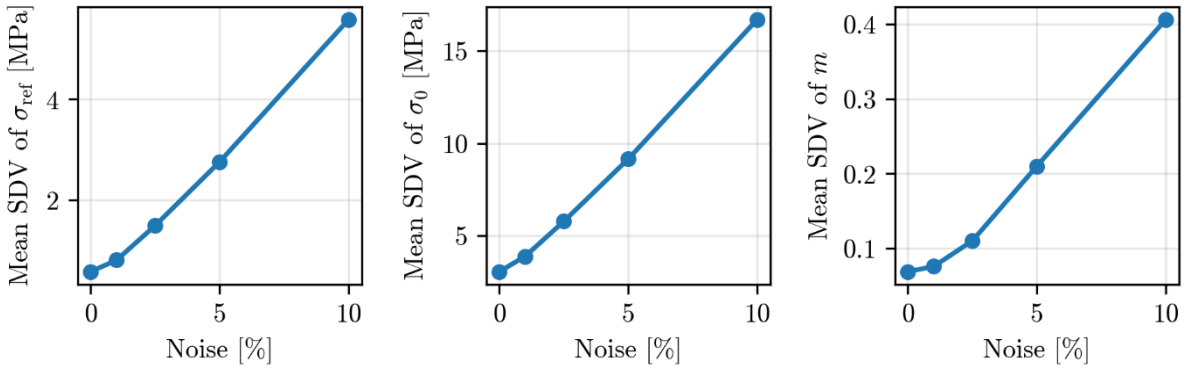


Figure 22. Parameter uncertainty in terms of mean standard deviation at various noise levels.

The predictive robustness of the identified constitutive parameters' response $Q_{k,i,r}^{pred,(s)}$ is assessed against the original noise free experimental response $Q_{k,i}^{exp}$. For client k, the root-mean square error for realization r at noise level s is calculated as

$$RMSE_{k,r}^{(s)} = \sqrt{\frac{1}{N_k}\sum_{i=1}^{N_k}\left[Q_{k,i,r}^{pred,(s)} - Q_{k,i}^{exp}\right]^2} \tag{55}$$

where N_k denotes the number of experimental observations. The mean prediction error at each noise level is subsequently obtained by averaging the RMSE values over the independent realizations.

The RMSE variation with noise level in Figure 23 indicates that prediction errors increase gradually as the imposed measurement noise becomes stronger, but the sensitivity differs across clients. Client 1 is the most affected, with the highest RMSE at all noise levels, increasing from about 16 MPa in the clean case to approximately 32 MPa at 10% noise, indicating strong variability across noise realizations. Clients 2 and 3 show moderate sensitivity, with RMSE values rising to roughly 18 MPa and 14 MPa, respectively, at 10% noise. In contrast, Clients 4 and 5 remain comparatively robust, with final RMSE values below about 9 MPa even at the highest noise level. The increasing error bars, particularly for Clients 1, indicate that higher noise not only increases the average prediction error but also makes the identified response more dependent on the particular noise realization.

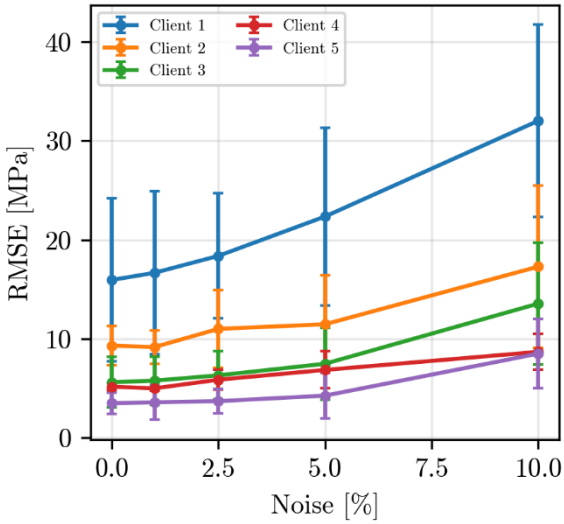


Figure 23. RMSE calculated against clean experimental data for noise levels

Finally, the uncertainty in the predicted constitutive response is represented using empirical 95% prediction intervals. At each deformation level $\varepsilon_{s,i}$, the predictions obtained from the R independent noise realizations form the set $\left\{Q_{k,i,1}^{pred,(s)}, Q_{k,i,2}^{pred,(s)}, \dots, Q_{k,i,R}^{pred,(s)}\right\}$. The lower and upper bounds of the empirical 95% prediction interval are defined by the 2.5th and 97.5th percentiles of this distribution as

$$Q_{k,i,lower}^{(s)} = \mathcal{P}_{2.5}\left(Q_{k,i,r}^{pred,(s)}\right)$$
$$Q_{k,i,upper}^{(s)} = \mathcal{P}_{97.5}\left(Q_{k,i,r}^{pred,(s)}\right) \quad (56)$$

where $\mathcal{P}_q(\cdot)$ denotes the q^{th} empirical percentile over the repeated noise realizations. The resulting interval therefore characterizes the variation in the predicted torsional response arising from measurement noise propagated through the federated inverse-identification procedure.

The prediction-band results in Figure 24 show that the I-FedSciML framework preserves the main torsional response trends under increasing noise measurement. In the clean case ($s = 0$), the 95% prediction intervals are essentially negligible, and the mean predictions closely follow the experimental torque–strain curves for all five clients. At $s = 5\%$, the uncertainty bands become visible but remain narrow over most of the deformation range, while the mean

predictions still reproduce the nonlinear hardening behavior of five clients. At $s = 10\%$, the prediction intervals widen noticeably, especially at larger ε_s, where uncertainty accumulates as the response magnitude increases. This effect is most pronounced for the higher-response clients, such as Client 1, where Q/a^3 reaches above 600 MPa, and for Clients 3–5, where the upper and lower bounds separate more clearly at high strain levels. Despite this increased spread, the clean experimental points generally remain within or close to the empirical 95% intervals, and the mean predictions continue to capture the overall torque–twist shape.

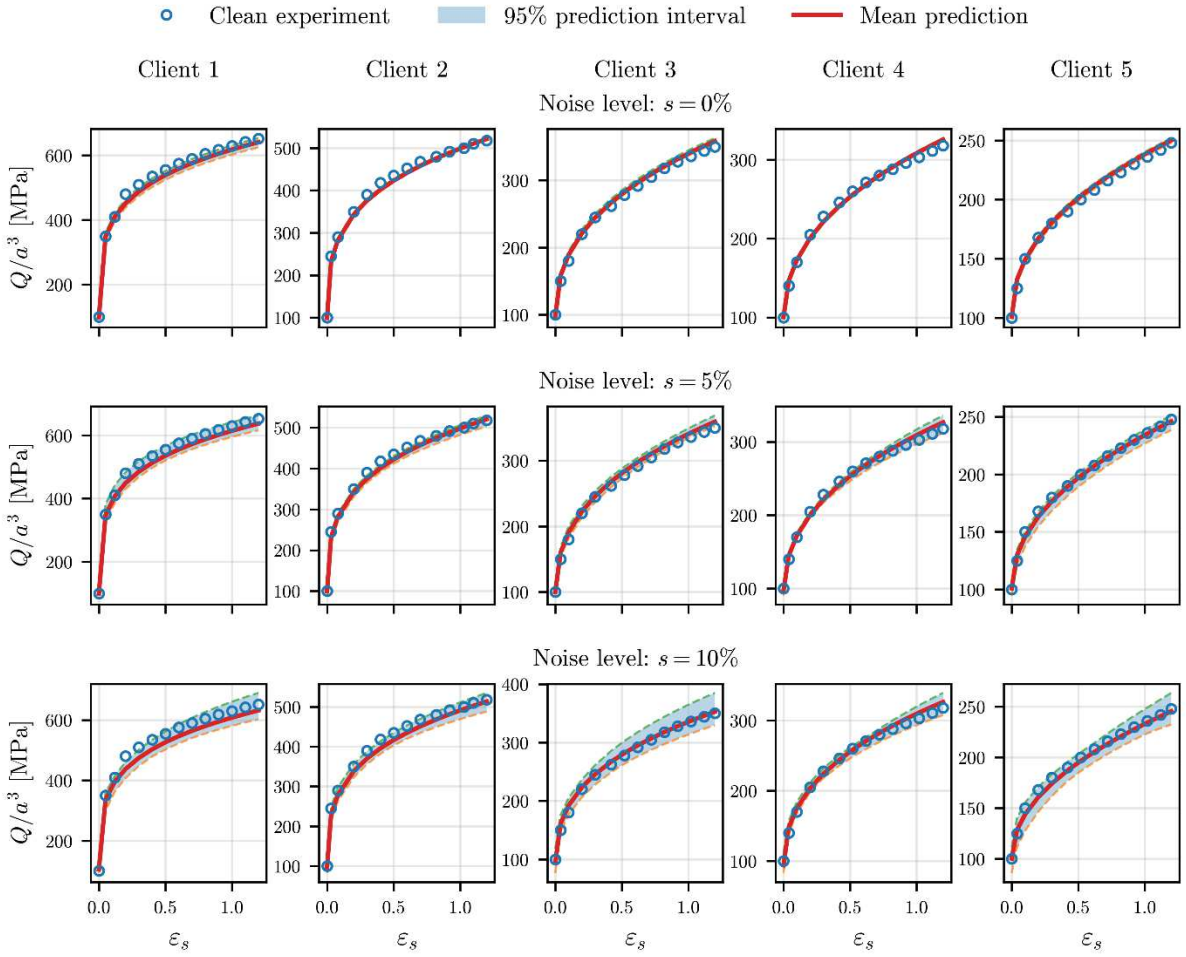


Figure 24. Predicted copper micro-torsion responses with uncertainty bands under different noise levels

The overall convergence history during federated training is presented in Figure 25. It shows that the loss decreases rapidly for all noise levels during the early communication rounds and then reaches a stable plateau. The clean case ($s = 0$) attains the lowest final relative MSE of $2\text{x}10^{-4}$, while 1% and 2.5% noise cases remain close to the clean response. The 5% noise case converges to a higher plateau near $2\text{x}10^{-3}$. On the other hand, the 10% noise case shows the largest final loss around 10^{-2}, and also exhibits the widest uncertainty band, reflecting greater variability across repeated noise realizations.

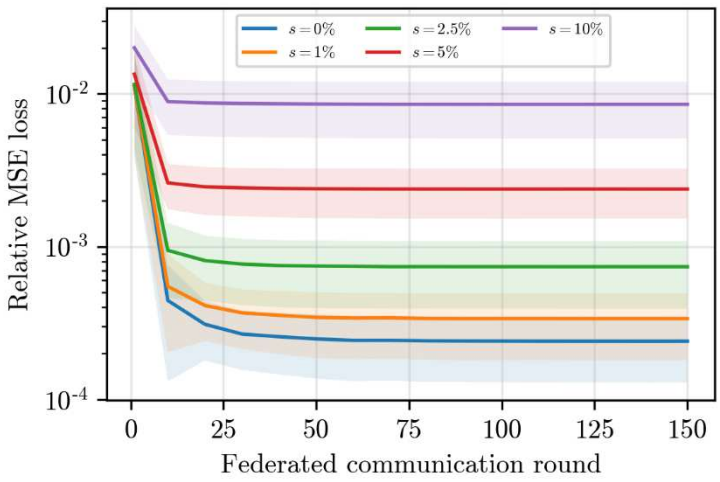


Figure 25. Convergence of federated training for $s = 0.0, 0.01, 0.025, 0.05, 0.1$

Overall, the results in this section demonstrate that the proposed I-FedSciML framework remains stable and reasonably robust under low-to-moderate noise measurement. As the noise level increases, the prediction intervals become wider and the attainable loss plateau rises, indicating greater uncertainty in the identified response. Nevertheless, even under the highest noise level considered, the framework preserves the main size-dependent torsional trends and maintains physically meaningful predictions. This suggests that I-FedSciML can tolerate realistic measurement perturbations while retaining its capability for reliable inverse identification of nonlocal SGP parameters.

5. Concluding Remarks and Future Work

In this study, we set out to address some of the challenges associated with the inverse calibration of non-local gradient plasticity models from micro-scale experiments. The central difficulty is that SGP models are governed by material parameters that are not directly measurable yet strongly influence the predicted size-dependent response. Conventional calibration procedures usually treat each experiment independently, which limits information sharing across geometrically distinct datasets and may lead to non-unique parameter sets. Therefore, we developed an inverse federated scientific machine learning framework in which each experimental curve is treated as an independent client, while a shared inverse model collaboratively learns the relationship between geometric descriptors and SGP model parameters.

The proposed framework combines three essential components: a geometry-conditioned inverse neural network, a differentiable physics-based SGP forward model, and a federated optimization strategy based on local client training and server-side weighted aggregation. Instead of using the neural network as a direct black-box predictor of the experimental response, the network is used to infer the SGP parameter vector for each client. These parameters are then passed through the SGP forward model to compute the predicted micro-bending or micro-torsion response.

The effectiveness of the framework was demonstrated using several benchmark micro-scale datasets, including micro-bending of thin annealed nickel beams, micro-bending of LIGA nickel foils, micro-bending of aluminum beams, and micro-torsion of thin copper wires. Across these cases, the I-FedSciML framework successfully identified client-specific SGP parameters while respecting the prescribed physical bounds. The predicted moment–curvature and torque–twist responses showed good agreement with the experimental measurements, and the obtained error metrics confirmed that the main size-dependent trends were accurately captured. The round-wise prediction plots further showed that the federated model progressively improves as communication proceeds.

The results also provide useful physical insight into parameter identifiability. In some cases, such as the annealed nickel and aluminum micro-bending examples, σ_{ref} converged close to its lower bound, suggesting that this parameter has limited sensitivity in distinguishing the corresponding bending responses. In contrast, the hardening modulus σ_0 and hardening exponent m showed stronger client-dependent variation, indicating that they play a more dominant role in adapting the SGP response to different geometries. For the LIGA nickel and copper micro-torsion datasets, more pronounced coupling among σ_{ref}, σ_0, and m was observed during federated training, highlighting the complexity of inverse identification in heterogeneous micro-scale experiments.

The robustness analysis of the framework conducted under different noise levels (1%, 2.5%, 5%, 10%) showed that the framework maintains stable convergence and reliable predictive capability under low-to-moderate measurement perturbations. As the noise level increased, the parameter bias, prediction uncertainty, and final loss plateau also increased, indicating that stronger noise is propagated through the inverse identification process. Nevertheless, even at the highest noise level of 10%, the framework preserved the main size-dependent torsional trends and produced physically meaningful client-specific responses.

The significance of this work also lies in the way it connects federated learning with physically grounded constitutive modeling. Many scientific and engineering datasets are distributed across different laboratories, institutions, materials, and testing conditions. In such settings, direct sharing of raw data may be restricted by privacy, ownership, or practical limitations. The proposed I-FedSciML framework offers a path toward collaborative constitutive model calibration without requiring centralized data storage. Hence, each client retains its own experimental data locally, while the shared inverse model learns from all clients through communicated model weights.

Looking forward, the framework can be extended in several important directions. First, additional physical constraints and regularization terms may be incorporated to improve parameter identifiability, especially in cases where different parameter combinations produce similar mechanical responses. Second, the current geometry-conditioned mapping can be expanded to include richer descriptors, such as grain morphology, crystallographic texture, strain-rate effects or temperature. Third, the same federated inverse strategy can be generalized beyond micro-bending and micro-torsion to other nonlocal and higher-order constitutive models, including coupled damage-plasticity, viscoplasticity, and gradient-enhanced fracture formulations. In this sense, the present study establishes a foundation for federated inverse modeling of size-dependent material behavior.

Statements and Declarations

Funding: This research did not receive any specific grant from the funding agencies in the public, commercial, or not-for-profit sectors.

Declaration of competing interest: The authors declare that they have no known competing financial interests or personal relationships that could have appeared to influence the work reported in this paper

Availability of data and materials: Some or all data that supports this study's findings are available from the corresponding author upon reasonable request

References

1. Aifantis, E. C. (1984). On the microstructural origin of certain inelastic models. Journal of Engineering Materials and Technology, 106(4), 326-330.
2. Alfano, G., Greco, S., Mandaglio, D., Parisi, F., Shahbazian, R., & Trubitsyna, I. (2025). Decentralized federated learning meets Physics-Informed Neural Networks. Knowledge-Based Systems, 323, 113717.
3. Al-Rub, R. K. A., & Voyiadjis, G. Z. (2006). A physically based gradient plasticity theory. International Journal of Plasticity, 22(4), 654-684.
4. Andrade-Campos, A., Bastos, N., Conde, M., Gonçalves, M., Henriques, J., Lourenço, R., & Rumor, L. (2022, May). On the inverse identification methods for forming plasticity models using full-field measurements. In IOP Conference Series: Materials Science and Engineering (Vol. 1238, No. 1, p. 012059). IOP Publishing.
5. As'ad, F., Avery, P., & Farhat, C. (2022). A mechanics-informed artificial neural network approach in data-driven constitutive modeling. International Journal for Numerical Methods in Engineering, 123(12), 2738-2759.
6. Bardella, L., & Panteghini, A. (2015). Modelling the torsion of thin metal wires by distortion gradient plasticity. Journal of the Mechanics and Physics of Solids, 78, 467-492.
7. Bastos, N., Prates, P. A., & Andrade-Campos, A. (2022). Material parameter identification of elastoplastic constitutive models using machine learning approaches. Key Engineering Materials, 926, 2193-2200.
8. Begley, M. R., & Hutchinson, J. W. (1998). The mechanics of size-dependent indentation. Journal of the Mechanics and Physics of Solids, 46(10), 2049-2068.
9. Blaysat, B., Florentin, E., Lubineau, G., & Moussawi, A. (2012). A Dissipation Gap Method for full-field measurement-based identification of elasto-plastic material parameters. International journal for numerical methods in engineering, 91(7), 685-704.
10. Cai, S., Mao, Z., Wang, Z., Yin, M., & Karniadakis, G. E. (2021). Physics-informed neural networks (PINNs) for fluid mechanics: A review. Acta Mechanica Sinica, 37(12), 1727-1738.

11. Claire, D., Hild, F., & Roux, S. (2004). A finite element formulation to identify damage fields: the equilibrium gap method. International journal for numerical methods in engineering, 61(2), 189-208.
12. Deliktaş, B., Tariq, A., Kurt, G., & Uygur, A. (2026). Developing a Vertical Federated Machine Learning Framework for Predicting Energy Consumption in Wastewater Treatment Plants: A Case Study of Melbourne. International Journal of Environmental Research, 20(2), 92.
13. Dorgan, R. J., & Voyiadjis, G. Z. (2003). Nonlocal dislocation based plasticity incorporating gradients of hardening. Mechanics of materials, 35(8), 721-732.
14. Faghihi, D., & Voyiadjis, G. Z. (2012). Determination of nanoindentation size effects and variable material intrinsic length scale for body-centered cubic metals. Mechanics of Materials, 44, 189-211.
15. Flaschel, M., Kumar, S., & De Lorenzis, L. (2021). Unsupervised discovery of interpretable hyperelastic constitutive laws. Computer Methods in Applied Mechanics and Engineering, 381, 113852.
16. Flaschel, M., Kumar, S., & De Lorenzis, L. (2023). Automated discovery of generalized standard material models with EUCLID. Computer Methods in Applied Mechanics and Engineering, 405, 115867.
17. Fleck, N. A., & Hutchinson, J. (1993). A phenomenological theory for strain gradient effects in plasticity. Journal of the Mechanics and Physics of Solids, 41(12), 1825-1857.
18. Fleck, N. A., & Hutchinson, J. W. (1997). Strain gradient plasticity. Advances in applied mechanics, 33, 295-361.
19. Fleck, N. A., Muller, G. M., Ashby, M. F., & Hutchinson, J. W. (1994). Strain gradient plasticity: theory and experiment. Acta Metallurgica et materialia, 42(2), 475-487.
20. Gan, Z., He, Y., Liu, D., Zhang, B., & Shen, L. (2014). Hall–Petch effect and strain gradient effect in the torsion of thin gold wires. Scripta Materialia, 87, 41-44.
21. Gao, H. H. Y. N. W., Huang, Y., Nix, W. D., & Hutchinson, J. (1999). Mechanism-based strain gradient plasticity—I. Theory. Journal of the Mechanics and Physics of Solids, 47(6), 1239-1263.
22. Gaynutdinova, L., Rokoš, O., Havelka, J., Pultarová, I., & Zeman, J. (2023). Bayesian approach to micromechanical parameter identification using Integrated Digital Image Correlation. International Journal of Solids and Structures, 280, 112388.
23. Grédiac, M. (1989). Principe des travaux virtuels et identification. Comptes rendus de l'Académie des sciences. Série 2, Mécanique, Physique, Chimie, Sciences de l'univers, Sciences de la Terre, 309(1), 1-5.
24. Gudmundson, P. (2004). A unified treatment of strain gradient plasticity. Journal of the Mechanics and Physics of Solids, 52(6), 1379-1406.
25. Guo, S., He, Y., Lei, J., Li, Z., & Liu, D. (2017). Individual strain gradient effect on torsional strength of electropolished microscale copper wires. Scripta Materialia, 130, 124-127.
26. Gurtin, M. E., & Anand, L. (2005). A theory of strain-gradient plasticity for isotropic, plastically irrotational materials. Part I: Small deformations. Journal of the Mechanics and Physics of Solids, 53(7), 1624-1649.
27. Haque, M. A., & Saif, M. T. A. (2003). Strain gradient effect in nanoscale thin films. Acta Materialia, 51(11), 3053-3061.

28. Huang, Y., Gao, H., Nix, W. D., & Hutchinson, J. (2000). Mechanism-based strain gradient plasticity—II. Analysis. Journal of the Mechanics and Physics of Solids, 48(1), 99-128.
29. Kadioglu, H. G., Tariq, A., Deliktas, B., & Yayli, M. O. (2026). Investigation of the torsional dynamics of viscoelastic nanorod through Gaussian process-based surrogate modeling and semi-analytical approaches. Mechanics Based Design of Structures and Machines, 54(1), 2571730.
30. Kairouz, P., & McMahan, H. B. (2021). Advances and open problems in federated learning. Foundations and trends in machine learning, 14(1-2), 1-210.
31. Kapcı, C. I., Tariq, A., Yazıcı, M., Deliktaş, B., & Voyiadjis, G. Z. (2026). On the development of neural network and phenomenological constitutive models for polycarbonate under thermomechanical and impact loading: Experimental and numerical approaches. European Journal of Mechanics-A/Solids, 106181.
32. Karimireddy, S. P., Kale, S., Mohri, M., Reddi, S., Stich, S., & Suresh, A. T. (2020, November). Scaffold: Stochastic controlled averaging for federated learning. In International conference on machine learning (pp. 5132-5143). PMLR.
33. Kavanagh, K. T., & Clough, R. W. (1971). Finite element applications in the characterization of elastic solids. International Journal of Solids and Structures, 7(1), 11-23.
34. Kirchdoerfer, T., & Ortiz, M. (2016). Data-driven computational mechanics. Computer Methods in Applied Mechanics and Engineering, 304, 81-101.
35. Ladèveze, P., & Leguillon, D. (1983). Error estimate procedure in the finite element method and applications. SIAM journal on numerical analysis, 20(3), 485-509.
36. Li, L., Fan, Y., Tse, M., & Lin, K. Y. (2020b). A review of applications in federated learning. Computers & Industrial Engineering, 149, 106854.
37. Li, T., Sahu, A. K., Zaheer, M., Sanjabi, M., Talwalkar, A., & Smith, V. (2020a). Federated optimization in heterogeneous networks. Proceedings of Machine learning and systems, 2, 429-450.
38. Ling, S., Wu, Z., Mei, J., & Lv, S. (2024). An efficient machine learning-based model for predicting the stress-strain relationships of thermoplastic polymers with limited testing data. Composites Part B: Engineering, 283, 111600.
39. Liu, D., He, Y., Dunstan, D. J., Zhang, B., Gan, Z., Hu, P., & Ding, H. (2013). Toward a further understanding of size effects in the torsion of thin metal wires: an experimental and theoretical assessment. International Journal of Plasticity, 41, 30-52.
40. Liu, D., He, Y., Tang, X., Ding, H., Hu, P., & Cao, P. (2012). Size effects in the torsion of microscale copper wires: Experiment and analysis. Scripta Materialia, 66(6), 406-409.
41. Lourenço, R., Tariq, A., Georgieva, P., Andrade-Campos, A., & Deliktaş, B. (2025). On the use of physics-based constraints and validation KPI for data-driven elastoplastic constitutive modelling. Computer Methods in Applied Mechanics and Engineering, 437, 117743.
42. Martínez-Pañeda, E., & Niordson, C. F. (2016). On fracture in finite strain gradient plasticity. International Journal of Plasticity, 80, 154-167.
43. Martins, J. M. P., Andrade-Campos, A., & Thuillier, S. (2018). Comparison of inverse identification strategies for constitutive mechanical models using full-field measurements. International Journal of Mechanical Sciences, 145, 330-345.

44. McMahan, B., Moore, E., Ramage, D., Hampson, S., & y Arcas, B. A. (2017, April). Communication-efficient learning of deep networks from decentralized data. In Artificial intelligence and statistics (pp. 1273-1282). Pmlr.
45. Moon, H., Park, D., Cho, H., Noh, H. K., Lim, J. H., & Ryu, S. (2025). Physics-informed neural network-based discovery of hyperelastic constitutive models from extremely scarce data. Computer Methods in Applied Mechanics and Engineering, 446, 118258.
46. Moussawi, A., Lubineau, G., Florentin, E., & Blaysat, B. (2013). The constitutive compatibility method for identification of material parameters based on full-field measurements. Computer methods in applied mechanics and engineering, 265, 1-14.
47. Mozaffar, M., Bostanabad, R., Chen, W., Ehmann, K., Cao, J., & Bessa, M. A. (2019). Deep learning predicts path-dependent plasticity. Proceedings of the National Academy of Sciences, 116(52), 26414-26420.
48. Niordson, C. F., & Hutchinson, J. W. (2003). Non-uniform plastic deformation of micron scale objects. International journal for numerical methods in engineering, 56(7), 961-975.
49. Nix, W. D., & Gao, H. (1998). Indentation size effects in crystalline materials: a law for strain gradient plasticity. Journal of the Mechanics and Physics of Solids, 46(3), 411-425.
50. Polat, A., Kurt, G., Tariq, A., Deliktaş, B., Yazıcı, M., & Voyiadjis, G. Z. (2026). A Validated Computational Framework for Investigating the Manufacturing Heterogeneities Induced from Injection Molding. International Journal of Mechanical Sciences, 111711.
51. Polat, A., Tariq, A., Deliktaş, B., Yazıcı, M., & Voyiadjis, G. Z. (2025). On the machine learning approach for computational homogenization of short fiber-reinforced composites with elastoplastic behavior. Journal of Reinforced Plastics and Composites, 07316844251371511.
52. Raissi, M., Perdikaris, P., & Karniadakis, G. E. (2019). Physics-informed neural networks: A deep learning framework for solving forward and inverse problems involving nonlinear partial differential equations. Journal of Computational physics, 378, 686-707.
53. Réthoré, J. (2010). A fully integrated noise robust strategy for the identification of constitutive laws from digital images. International Journal for Numerical Methods in Engineering, 84(6), 631-660.
54. Reddi, S., Charles, Z., Zaheer, M., Garrett, Z., Rush, K., Konečný, J., & McMahan, H. B. (2020). Adaptive federated optimization. arXiv preprint arXiv:2003.00295.
55. Rezaei, S., Moeineddin, A., & Harandi, A. (2024). Learning solutions of thermodynamics-based nonlinear constitutive material models using physics-informed neural networks. Computational Mechanics, 74(2), 333-366.
56. Seidl, D. T., & Granzow, B. N. (2022). Calibration of elastoplastic constitutive model parameters from full-field data with automatic differentiation-based sensitivities. International Journal for Numerical Methods in Engineering, 123(1), 69-100.
57. Shrotriya, P., Allameh, S. M., Lou, J., Buchheit, T., & Soboyejo, W. O. (2003). On the measurement of the plasticity length scale parameter in LIGA nickel foils. Mechanics of materials, 35(3-6), 233-243.
58. Song, Y., & Voyiadjis, G. Z. (2018). Small scale volume formulation based on coupled thermo-mechanical gradient enhanced plasticity theory. International Journal of Solids and Structures, 134, 195-215.
59. Stölken, J. S., & Evans, A. G. (1998). A microbend test method for measuring the plasticity length scale. Acta Materialia, 46(14), 5109-5115.

60. Tariq, A., & Deliktaş, B. (2025). An inverse parameter identification in finite element problems using machine learning-aided optimization framework. Experimental Mechanics, 65(3), 325-349.
61. Tariq, A., Deliktaş, B., & Voyiadjis, G. Z. (2026). Thermodynamically consistent physics-informed neural network approach for thin films with nonstandard boundary conditions. Thin-Walled Structures, 114743.
62. Tariq, A., Kadıoğlu, H. G., Uzun, B., Deliktaş, B., & Yaylı, M. Ö. (2025). Semi-analytical and machine learning approaches for investigating the torsional vibration behavior of nano-sized viscoelastic tubes. Mechanics of Advanced Materials and Structures, 1-21.
63. Tariq, A., Uzun, B., Deliktaş, B., & Yaylı, M. Ö. (2024). Assessment of machine learning methods predicting the axial vibration frequencies of microbars. ZAMM-Journal of Applied Mathematics and Mechanics/Zeitschrift Für Angewandte Mathematik Und Mechanik, 104(3), e202300916.
64. Thakolkaran, P., Joshi, A., Zheng, Y., Flaschel, M., De Lorenzis, L., & Kumar, S. (2022). NN-EUCLID: Deep-learning hyperelasticity without stress data. Journal of the Mechanics and Physics of Solids, 169, 105076.
65. Voyiadjis, G. Z., & Kattan, P. I. (1992). Finite elasto-plastic analysis of torsion problems using different spin tensors. International journal of plasticity, 8(3), 271-314.
66. Voyiadjis, G. Z., & Al-Rub, R. K. A. (2005). Gradient plasticity theory with a variable length scale parameter. International Journal of solids and structures, 42(14), 3998-4029.
67. Voyiadjis, G. Z., & Deliktas, B. (2009). Formulation of strain gradient plasticity with interface energy in a consistent thermodynamic framework. International Journal of Plasticity, 25(10), 1997-2024.
68. Voyiadjis, G. Z., & Faghihi, D. (2014). Overview of enhanced continuum theories for thermal and mechanical responses of the microsystems in the fast-transient process. Journal of Engineering Materials and Technology, 136(4), 041003.
69. Voyiadjis, G., & Al-Rub, R. K. A. (2007). Nonlocal gradient-dependent thermodynamics for modeling scale-dependent plasticity. international Journal for Multiscale computational Engineering, 5(3-4).
70. Voyiadjis, G. Z., Znemah, R. A., & Wood, P. (2023). Microstructure and geometry effects on the compressive behavior of LPBF-manufactured inconel 718 honeycomb structures. Journal of Materials Research and Technology, 24, 1562-1578.
71. Voyiadjis, G. Z., & Song, Y. (2019). Strain gradient continuum plasticity theories: theoretical, numerical and experimental investigations. International Journal of Plasticity, 121, 21-75.
72. Wang, J. L., Fu, M. W., Shi, S. Q., & Korsunsky, A. M. (2018). Influence of size effect and plastic strain gradient on the springback behaviour of metallic materials in microbending process. International Journal of Mechanical Sciences, 146, 105-115.
73. Wen, J., Zhang, Z., Lan, Y., Cui, Z., Cai, J., & Zhang, W. (2023). A survey on federated learning: challenges and applications. International journal of machine learning and cybernetics, 14(2), 513-535.
74. Xie, J., Javili, A., & Linder, C. (2025). The Kirsch problem in second strain gradient elasticity. Proceedings of the Royal Society A, 481(2319), 20250389.

75. Yang, Q., Liu, Y., Chen, T., & Tong, Y. (2019). Federated machine learning: Concept and applications. ACM Transactions on Intelligent Systems and Technology (TIST), 10(2), 1-19.
76. Yun, G. J., & Shang, S. (2011). A self-optimizing inverse analysis method for estimation of cyclic elasto-plasticity model parameters. International Journal of Plasticity, 27(4), 576-595.
77. Zhang, C., Xie, Y., Bai, H., Yu, B., Li, W., & Gao, Y. (2021). A survey on federated learning. Knowledge-Based Systems, 216, 106775.
78. Zhang, H., Liu, L., Weng, K., & Lu, L. (2025). Federated scientific machine learning for approximating functions and solving differential equations with data heterogeneity. IEEE Transactions on Neural Networks and Learning Systems.